

**RADAR RANGE-DOPPLER IMAGING USING JOINT TIME-  
FREQUENCY TECHNIQUES**

**A THESIS SUBMITTED TO  
THE GRADUATE SCHOOL OF NATURAL AND APPLIED SCIENCES  
OF  
THE MIDDLE EAST TECHNICAL UNIVERSITY**

**BY**

**DENİZ AKHANLI**

**IN PARTIAL FULFILLMENT OF THE REQUIREMENTS  
FOR  
THE DEGREE OF MASTER OF SCIENCE  
IN  
ELECTRICAL AND ELECTRONICS ENGINEERING**

**APRIL 2007**

Approval of the Graduate School of Natural and Applied Sciences

---

Prof. Dr. Canan ÖZGEN

Director

I certify that this thesis satisfies all the requirements as a thesis for the degree of Master of Science.

---

Prof. Dr. İsmet ERKMEN

Head of Department

This is to certify that we have read this thesis and that in our opinion it is fully adequate, in scope and quality, as a thesis for the degree of Master of Science.

---

Prof. Dr. Gülbin DURAL

Supervisor

Examining Committee Members

Prof. Dr. Mustafa KUZUOĞLU (METU) \_\_\_\_\_

Prof. Dr. Gülbin DURAL (METU) \_\_\_\_\_

Prof. Dr. Kemal LEBLEBİCİOĞLU (METU) \_\_\_\_\_

Assoc. Prof. Dr. S. Sencer KOÇ (METU) \_\_\_\_\_

Assoc. Prof. Dr. Birsen SAKA (Hacettepe Univ.) \_\_\_\_\_

**I hereby declare that all information in this document has been obtained and presented in accordance with academic rules and ethical conduct. I also declare that, as required by these rules and conduct, I have fully cited and referenced all material and results that are not original to this work.**

Name, Last name: Deniz AKHANLI

Signature:

## **ABSTRACT**

### **RADAR RANGE-DOPPLER IMAGING USING JOINT TIME-FREQUENCY TECHNIQUES**

**Akhanlı, Deniz**

M.S., Department of Electrical and Electronics Engineering

Supervisor: Prof. Dr. Gülbin Dural

April 2007, 89 pages

Inverse Synthetic Aperture Radar coherently processes the return signal from the target in order to construct the image of the target. The conventional methodology used for obtaining the image is the Fourier transform which is not capable of suppressing the Doppler change in the return signal. As a result, Range-Doppler image is degraded. A proper time-frequency transform suppresses the degradation due to time varying Doppler shift.

In this thesis, high resolution joint-time frequency transformations that can be used in place of the conventional method are evaluated. Wigner-Ville Distribution, Adaptive Gabor Representation with Coarse-to-Fine search algorithm, and Time-Frequency Distribution Series are examined for the target imaging system.

The techniques applied to sample signals compared with each other. The computational and memorial complexity of the methods are evaluated and

compared to each other and possible improvements are discussed. The application of these techniques in the target imaging system is also performed and resulting images compared to each other.

Keywords: Inverse Synthetic Aperture Radar, Joint Time-Frequency Transform, Wigner-Ville Distribution, Adaptive Gaussian Representation, Time-Frequency Distribution Series

# ÖZ

## TÜMLEŞİK ZAMAN-SIKLIK DÖNÜŞÜMLERİ KULLANARAK RADAR MENZİL-DOPPLER GÖRÜNTÜLEME

**Akhanlı, Deniz**

Yüksek Lisans, Elektrik Elektronik Mühendisliği Bölümü

Tez Yöneticisi: Prof. Dr. Gülbin DURAL

Nisan 2007, 89 sayfa

Ters Yapay Ağız Aralıklı Radar, hedefin görüntüsünü oluşturmak için hedeften dönen işaretleri eş evreli olarak işler. Hedefin görüntüsü elde etmek için kullanılan geleneksel yöntem Fourier dönüşümüdür. Fourier dönüşümü dönen işaretlerdeki Doppler değişimini bastırma yetisine sahip değildir. Bunun sonucu olarak menzil-Doppler görüntüsü bozulur. Uygun bir zaman-sıklık dönüşümü zamanla değişen Doppler değişimi sebebiyle oluşan bozulmayı bastırır.

Bu tez çalışmasında, geleneksel metodun yerine kullanılabilecek zaman-çevrim dönüşümleri değerlendirilmiştir. Hedef görüntüleme sistemleri için Wigner-Ville dağılımı, Kabadan İnceye Arama ile Uyarlamalı Gabor Gösterimi ve Zaman-Çevrim Dağılım Sıralamaları incelenmiştir.

Teknikler örnek işaretlere uygulanmış ve sonuçlar birbirleri ile karşılaştırılmıştır. Tekniklerin işlemsel ve hafızasal karmaşıklığı bulunmuş, sonuçlar karşılaştırılmış ve olası geliştirmeler önerilmiştir. Tekniklerin

hedef görüntüleme sistemindeki uygulamaları taklit hedef kullanılarak gerçekleştirilmiş ve elde edilen görüntüler birbirleri ile karşılaştırılmıştır.

Anahtar Kelimeler: Ters Yapay Ağız Aralıklı Radar, Tümlşik zaman-çevrim dönüşümleri, Wigner-Ville Dağılımı, Uyarlamalı Gabor Gösterimi, Zaman-Çevrim Dağılım Sıralamaları

*All is the same,  
Time has gone by,  
Someday you come,  
Someday you'll die  
Somebody has died  
Long time ago*

*C. Pevease*

## ACKNOWLEDGEMENTS

First and mostly, I would like to thank to my supervisor, Prof. Dr. Glbin DURAL for her support, encouragement and belief throughout the study. Without her guiding light, I would totally be lost and drawn in the whirlpools of the large sea of science.

Aselsan is a very special company to work for. I would like to thank to everyone in my department for their friendly attitude, especially Caner TEZEL, Erkan ANKAYA and Ali DEMİRCİ for their warm friendship.

Very special thanks to the Swedish jazz trio E.S.T. and their wonderful music. Their music has turned the “have to study” times to a wonderland.

Bora KAT, my home-mate, is a very special friend who thought me the meaning of being a true scholar.

Başak SAKARYA gave me the reason to continue, reason to believe and reason to love. Thank you Başak, without you none of those were possible.

I wish to express my gratitude to my family for their support, patience and love in their eyes.

# TABLE OF CONTENTS

ABSTRACT.....	iv
ÖZ.....	vi
ACKNOWLEDGMENTS.....	ix
TABLE OF CONTENTS.....	x
LIST OF FIGURES.....	xii
CHAPTERS	
1. INTRODUCTION.....	1
1.1 Radar Imaging.....	1
1.1 Joint Time-Frequency Transforms.....	3
1.2 Outline of the Thesis.....	4
2. INVERSE SYNTHETIC APERTURE RADAR IMAGING SYSTEM.....	6
2.1 Introduction.....	6
2.2 Basic ISAR Theory.....	6
2.3 Conventional Range-Doppler Imaging.....	9
2.4 Stepped Frequency Modulated Radar.....	14
2.4 ISAR Data Simulation.....	17
3. JOINT TIME-FREQUENCY TRANSFORMATIONS FOR RADAR IMAGING.....	20
3.1 Introduction.....	20
3.2 Short Time Fourier Transform (STFT).....	22
3.3 Discrete Gabor Transform (DGT).....	28
3.4 Wigner-Ville Distribution (WVD).....	40

3.5 Adaptive Gaussian Representation (AGR).....	44
3.6 Time-Frequency Distribution Series (TFDS).....	53
4. APPLICATION OF JOINT TIME-FREQUENCY TRANSFORMS TO RADAR IMAGERY.....	61
4.1 Introduction.....	61
4.2 Radar Imaging Using Joint Time-Frequency Transforms.....	61
4.3 Results.....	62
4.3.1 Single Stationary Point Scatterer .....	63
4.3.2 Two Stationary Point Scatterers at Different Ranges.....	64
4.3.3 Two Point Scatterers at Different Cross Ranges.....	66
4.3.4 Rotating Mig-25 Simulation.....	69
4.3.5 Target with Translational Motion and Velocity Fluctuation.....	73
4.3.6 Measured Data Set.....	79
4.4 Comparison of the Methods.....	83
5. CONCLUSIONS .....	85
REFERENCES.....	87

# LIST OF FIGURES

## FIGURES

Figure 2.1 Cross-range resolution depends on antenna beam width .....	7
Figure 2.2 Fourier transform of received signal from two scatterers at same range with different velocities.....	11
Figure 2.3 Geometry of radar image of an object.....	11
Figure 2.4 Frequency of pulses over the integration time.....	15
Figure 2.5 Stepped-frequency ISAR imaging of a moving target.....	16
Figure 2.6 A point scatterer aircraft model.....	18
Figure 3.1 (a) Sample signal No.1 (b) Sample signal No. 2 (c) Sample signal No. 3.....	21
Figure 3.2 Bat Signal .....	22
Figure 3.3 STFT operation .....	23
Figure 3.4 Gaussian windows used in the computation of STFT .....	26
Figure 3.5 STFT of sample signal 2 with 1 <sup>st</sup> window function .....	27
Figure 3.6 STFT of sample signal 2 with 2 <sup>nd</sup> window function .....	27
Figure 3.7 Gaussian type curve is the analysis window. The other is its dual at the critical sampling.....	29
Figure 3.8 Periodic discrete Gabor analysis of sample signal no. 2 at critical sampling.....	33
Figure 3.9 Periodic discrete Gabor analysis of sample signal no. 2 at double oversampling.....	34
Figure 3.10 Periodic discrete Gabor analysis of sample signal no. 2 at quadruple oversampling.....	35
Figure 3.11 Bat signal using periodic discrete Gabor expansion with full resolution.....	35

Figure 3.12 Dual functions of Gaussian type signal at (a) double and (b) quadruple sampling.....	39
Figure 3.13 Dual functions of chirp type signal at (a) double and (b) quadruple sampling.....	39
Figure 3.14 WVD of sample signal no. 1.....	42
Figure 3.15 WVD of sample signal no. 3.....	43
Figure 3.16 WVD of bat signal.....	43
Figure 3.17 Computation procedure of adaptive representation.....	45
Figure 3.18 AGR of sample signals no.1, no.2, no.3 and bat signal.....	51
Figure 3.19 Convergence graphics for (a) sample signal no.1 (b) sample signal no. 2 (c) sample signal no. 3 and (d) bat signal.....	52
Figure 3.20 (a) TFDS of order 0, (b) TFDS of order 3 (c) P of order 5, (d) TFDS of order 5 (e) P of order 20 and (f) TFDS of order 20 for sample signal no. 1.....	56
Figure 3.21 (a) TFDS of order 0, (b) TFDS of order 3, (c) P of order 15 and (d) TFDS of order 15 of sample signal no. ....	58
Figure 3.22 (a) TFDS of order 0 and (b) TFDS of order 3 for sample signal no. 2.....	59
Figure 3.23 (a) TFDS of order 0, (b) TFDS of order 4 and (c) TFDS of order 20 for the bat signal.....	60
Figure 4.1 The structure of a radar imaging system with joint time-frequency transform.....	62
Figure 4.2 Range profile of single stationary point scatterer .....	63
Figure 4.3 Surface plot of the radar image of single stationary point scatterer using Fourier transform.....	64
Figure 4.4 Range profile of two stationary scatterers at different ranges..	65
Figure 4.5 Conventional radar image of two stationary scatterers at Different ranges.....	65
Figure 4.6 Range profiles of two scatterers at same range, separated 5m in cross-range, rotation rate is 3 deg/sec .....	67
Figure 4.7 Conventional image of two scatterers at same range, separated 5m in cross-range, rotation rate is 3 deg/ sec.....	67
Figure 4.8 Range profiles of two scatterers at same range, separated 5m	

in cross-range, rotation rate is 18 deg/sec .....	68
Figure 4.9 Conventional image of two scatterers at same range, separated 5m in cross-range, rotation rate is 18 deg/sec .....	68
Figure 4.10 Range profile for Mig-25 simulation.....	69
Figure 4.11 Image of Mig-25 simulation using Fourier Transform.....	70
Figure 4.12 Images of Mig-25 generated using AGR.....	71
Figure 4.13 Images of Mig-25 generated by using TFDS of order 3.....	72
Figure 4.14 Point scatterer model of an aircraft .....	74
Figure 4.15 Sketch of the initial position of the target .....	74
Figure 4.16 Speed of the target vs. Time .....	75
Figure 4.17 Range profile of target with fluctuating translational speed...75	
Figure 4.18 Image of target with fluctuating translational speed using Fourier Transform.....	76
Figure 4.19 Images of target with fluctuating translational speed using AGR.....	76
Figure 4.20 Images of target with fluctuating translational speed using TFDS of order 3.....	78
Figure 4.21 Range Profile of measured B727 aircraft.....	80
Figure 4.22 Image of measured B727 aircraft using Fourier Transform .....	80
Figure 4.23 Images of measured B727 aircraft using AGR.....	81
Figure 4.24 Images of measured B727 aircraft using TFDS of order 3.....	82

# CHAPTER 1

## INTRODUCTION

### 1.1 Radar Imaging

**Radio Detection and Ranging (RADAR)** is a system that uses radio waves to determine and map the location, direction, and/or speed of both moving and fixed objects such as aircraft, ships, motor vehicles, weather formations and terrain. It transmits electromagnetic energy to a target and receives the reflected signal from the target and clutter [1]. From the received signal, target related information such as location and velocity can be accurately measured. Therefore, there are many civilian and military areas where radar is extensively used [2].

In general, radar processes the received signal and extracts information about the target. The range to the target, i.e., the distance from the radar to the target measured along the radar line of sight, is estimated by measuring the time-delay between the transmitted signal and the received signal. For a moving target, the measurement of the target's velocity is based on the well-known Doppler effect. If the radar-transmitted signal is at frequency  $f$ , the reflected signal from the moving target is subject to Doppler frequency shift from its transmitted frequency,  $f + fd$ . This frequency shift is induced by relative motion between the radar and the target. In the case where a target has a radial velocity  $v$ , the Doppler

frequency shift is determined by the radial velocity of the target and the wavelength of the radar transmitted waveform [3].

Radar can achieve high resolution in range by employing a high bandwidth waveform to separate closely spaced radar scatterers on the target [4]. Moreover, by processing the received signal coherently, forming a synthetic aperture is possible as far as there exists a relative motion between the radar and the target [5]. Using this fact, resolution in the dimension perpendicular to the radar's line of sight can be increased [6].

Synthetic Aperture Radar (SAR) uses this technique in order to achieve the high resolution. In the SAR case, radar is moving to form the synthetic aperture. When the target is moving and the radar is stationary, Inverse Synthetic Aperture Radar (ISAR) uses the Doppler information from the different scattering mechanism to generate the high-resolution radar image.

Conventional ISAR imaging, which uses Fourier transform as the imaging methodology suffers from the image blurring and degradation due to the time-varying Doppler shifts of the scatterers if the target is not moving smoothly [1]. Several motion compensation methodologies are introduced to reduce this blurring and degradation [7], [8].

Another methodology to increase image quality is using joint time-frequency techniques in place of the conventional transform based imaging technique. The main advantage of the time-frequency transform is the instantaneous Doppler frequency shift can be calculated as a function of time and frequency. Therefore, image degradation due to Doppler shift of the scatterers are divided into different smaller time intervals and their effects are limited in the time interval specified by the

time resolution of the joint time-frequency transform [1]. In this thesis, two high-resolution joint time-frequency transforms are examined and applied to the ISAR imagery.

## **1.2 Joint Time-Frequency Transforms**

The most important and fundamental variables in signal processing are time and frequency. Traditionally, signals have been studied either as a function of time or as a function of frequency [9]. Joint time-frequency representation, on the other hand, represents the signals in both of the domains. The signals with time dependent power spectrum can be represented more powerfully.

The simplest form of the joint time frequency transforms is the Short Time Fourier Transform (STFT). In STFT, signal is divided into parts in time domain with a window function and Fourier transform of each part is taken. However, time and frequency resolutions in this representation are bounded by well known uncertainty principle. Therefore, obtaining satisfactory resolution results for signals in general is not possible [9].

Inverse of the sampled STFT is called Gabor expansion. Since the functions used while analysis and synthesis of STFT is not same, computing a dual function for Gabor expansion has to be studied. Using inverse Gabor expansion for infinite signals, generating a compact representation in joint time-frequency plane is possible with this method once the synthesis function is computed [10].

Wigner-Ville Distribution (WVD) possess high resolution in both time and frequency domains. However, if the signal under examination has more than one time or frequency components, this representation generates

oscillatory interference in between the parts of the signal. This effect is called cross-term interference and it has no physical meaning. However, it contributes to the useful characteristics of WVD such as instantaneous frequency, marginal time and frequency properties [1].

In order to remove the cross-term interference, several methodologies are proposed. Cohen's class examines the WVD in ambiguity plane and applies a kernel function to remove the cross term interference [9]. Adaptive Gaussian Representation (AGR) adaptively determines the elementary functions to identify the auto-terms [11]. Time Frequency Distribution Series (TFDS), uses discrete Gabor transform coefficients to identify the auto-terms on WVD plane and removes the cross-terms that causes image degradation while leaving the necessary ones in the representation [12].

In this study, STFT, DGT, WVD, AGR, and TFDS are studied and explained. Application of the AGR and TFDS to radar imagery is conducted and results are presented. Time consumed by these two joint time-frequency transforms is also evaluated and compared.

### **1.3 Outline of the Thesis**

Chapter 2 introduces ISAR image generation and related concepts. After defining range and cross-range resolution, direct radar imaging technique is briefly introduced. Conventional method used in the ISAR imaging is explored by deriving the Doppler resolution, and the mathematical form of radar return signal is derived and its relationship with Fourier transform is given. Also step frequency modulated radar and its simulation is basically given in chapter 2.

In chapter 3, joint time-frequency transforms are explained and evaluated using some sample signals. After introducing STFT, DGT is explained in detail. DGT is also one of the steps conducting TFDS. WVD and its properties are given in this chapter. Following WVD, two methodologies to remove the cross term interference is given, namely AGR and TFDS.

In chapter 4, applications of joint time-frequency methodologies are evaluated. After giving several simple examples of conventional imaging methods, joint time frequency imaging methods applied to two target models with different motion profiles. Moreover, the analysis for measured data set for Boeing 727 (B727) type aircraft is conducted. Finally, comparison of methodologies is given in the last part of this chapter.

Chapter 5 concludes the thesis.

## **CHAPTER 2**

# **INVERSE SYNTHETIC APERTURE RADAR IMAGING SYSTEM**

### **2.1 Introduction**

This chapter serves as a brief introduction to Inverse Synthetic Aperture Radar (ISAR) imaging.

### **2.2 Basic ISAR Theory**

The radar sensors respond to electromagnetic waves which are scattered when the propagation of incident waves is disturbed by the presence of an object. The physical mechanism can be described as follows: the incident fields induce currents in the volume bounded by the object to generate scattered fields, subject to constraints imposed by boundary conditions [14]. Using this response, radar detects the location of the targets such as aircrafts, ships and ground vehicles.

Range and cross-range resolution determines the quality of the radar image [15]. Range resolution can be defined as the ability of resolving point targets separated in range to the radar [13]. Two adjacent point

scatterers can be differentiated from each other if the reflected radar pulses from each can be received as two different pulses. Therefore, the radar range resolution is inversely proportional with the radar pulse width and directly proportional with the bandwidth of the radar pulse [14]. The expression for range resolution is given as [13]

$$\Delta r_r = \frac{c}{2\beta} \quad (2.1)$$

where  $\beta$  is the waveform band width and  $c$  is the speed of light.

Cross-range is the dimension perpendicular to the axis of the antenna. Therefore, cross-range resolution can be defined as the ability of identifying two different scatterers on the same range. Cross-range resolution is dependent on the antenna beam width. Figure 2.1 explains the concept of range resolution. The scatterers located in the beam at the same time can not be identified as different scatterers.

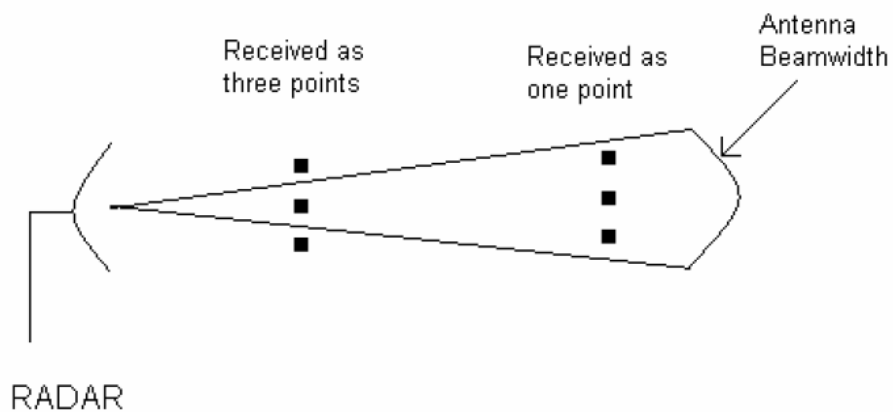


Figure 2.1: Cross-range resolution depends on antenna beam width.

Radar image can be defined as the spatial distribution of reflectivity corresponding to the object [14]. In the most direct form, radar imaging can be accomplished by using range-gated, short pulse radar with a pencil beam antenna. The systematic scanning of the volume by the radar beam and the range gate, radar image can be obtained without further processing. However, there are several disadvantages of this approach. First of all, Antenna beam width is inversely proportional to the antenna aperture size. Therefore, in order to obtain high cross-range resolution with this method, very large antenna apertures must be used. In addition, cross-range resolution decreases as the range increases because beam width also increases with range. Finally, several electromagnetic interactions are not visible when only a part of the target is illuminated [14].

Synthetic aperture processing is used in order to overcome those drawbacks of the direct imaging methods. Spatial resolution can be increased when results of many observations of the object at different frequencies and angles coherently combined [14]. Coherent processing maintains the relative phases of successive radar pulses. Thus, the phase from pulse to pulse is preserved and a phase correction can be applied to the returned signals to make them coherent for successive inter-pulse periods [1].

As long as there is a relative motion between the radar and the target, a synthetic aperture can be formed [1]. Synthetic Aperture Radar (SAR) uses synthetic processing techniques when the target is stationary and the radar is moving. Inverse Synthetic Aperture Radar (ISAR), on the other hand, does the same thing when the radar is stationary and the target is moving. ISAR uses the Doppler shift information to obtain the cross-range resolution. The differential Doppler shifts of adjacent scatterers of the

target can be observed; therefore, the distribution of the target's reflectivity can be measured by the Doppler spectra [14]. The distribution of the radar reflectivity can be measured by taking the Fourier transform over the observation time interval [3].

### 2.3 Conventional Range-Doppler Imaging

The conventional imaging on range-Doppler plane is achieved using Fourier transform. In order to use Fourier transform properly, some restrictions must be applied. During the imaging time, the scatterers must remain in their range cells and their Doppler frequency shifts must be constant [14].

Radar range resolution expression is given as Equation (2.1). Regardless of waveform, this relationship holds [13]. Cross-range resolution is improved using Doppler shifts as explained. Therefore, developing the expression for the Doppler resolution is beneficial. Doppler resolution refers to the ability of resolving scatterers moving at different radial velocity.

Assume that radar transmits a pulse of the form,

$$s_T(t) = \exp(j2\pi f_0 t) \quad (2.2)$$

The return signal from the target which moves with a velocity  $v_r$  in the radial direction, will be delayed version of the transmitted signal [14]. The amount of delay will depend on the range of the target.

$$s_R(t) = \exp(j2\pi f_0(t - \frac{2r(t)}{c})) \quad (2.3)$$

By taking the time derivative of the phase of the return signal, one may calculate the frequency of the signal [14].

$$f_r = \frac{1}{2\pi} \frac{\partial(2\pi f_0(t - \frac{2r(t)}{c}))}{\partial t} = f_0 - \frac{2f_0}{c} \frac{\partial r(t)}{\partial t} = f_0 - \frac{2f_0 v_r}{c} \quad (2.4)$$

Therefore, Doppler shift induced by a single scatterer can be written as,

$$f_D = \frac{2f_0 v_r}{c} = \frac{2v_r}{\lambda} \quad (2.5)$$

where  $\lambda$  is the wavelength. Since  $v_r$  is much smaller than speed of light,  $f_0$  is much larger than Doppler shift induced.

In order to derive the Doppler resolution, assume there are two identical scatterers at the same radial range but moving with different velocities,  $v_{r1}$  and  $v_{r2}$ . This time let the observation time is  $T_N$ . Received signal will be the sum of two responses from two scatterers. In order to resolve the two scatterers, their response in frequency domain should be identifiable one by one. Therefore their frequency shifts due to Doppler shifts must be separated by an amount of  $\frac{1}{T_N}$  as shown in Figure 2.2. Hence, this expression can be referred as Doppler resolution.

$$\Delta f_d = \frac{1}{T_N} \quad (2.6)$$

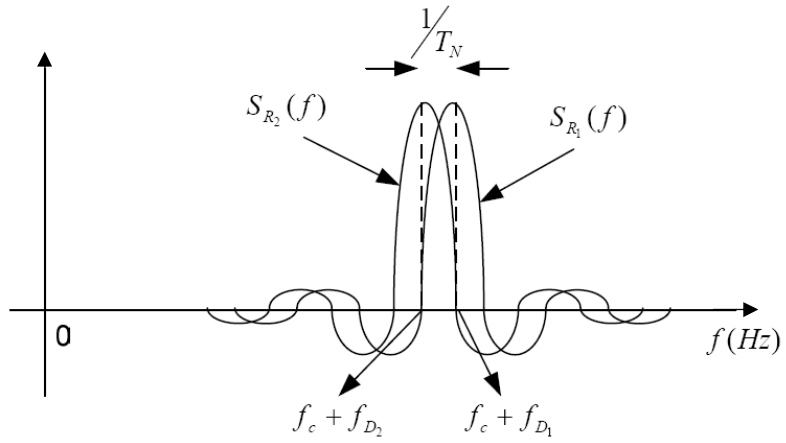


Figure 2.2: Fourier transform of received signal from two scatterers at same range with different velocities.

The geometry of the radar imaging of an object is shown on Figure 2.3.

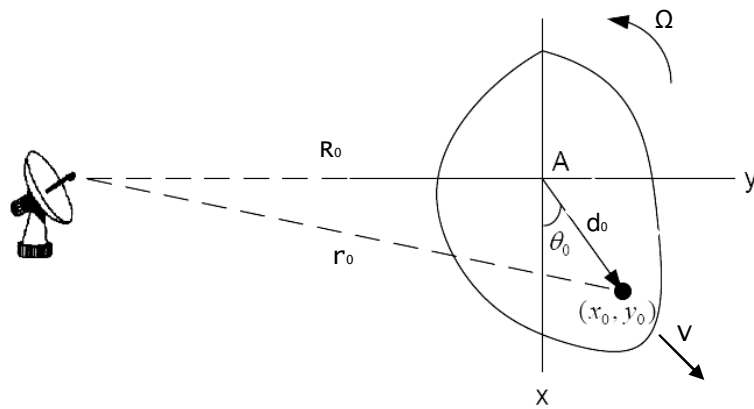


Figure 2.3: Geometry of radar image of an object

Assume at time  $t=0$ , a point scatterer on the target is located at  $(x_0, y_0)$ .  
The range of the point scatterer at this time can be calculated as,

$$r_0 = (R_0^2 + d_0^2 + 2d_0R_0 \sin(\Theta_0))^{1/2} \quad (2.7)$$

where  $d_0 = (x_0^2 + y_0^2)^{1/2}$  and  $\Theta_0 = \arctan(y_0/x_0)$ .

Assume radar transmitted signal is a sinusoidal waveform with carrier frequency  $f_c$ , that is,

$$s_T(t) = \exp(j2\pi f_c t) \quad (2.8)$$

The returned baseband signal is [1], then

$$s_R(t) = \rho(x_0, y_0) \exp(j2\pi f_c \frac{2r_0}{c}) \quad (2.9)$$

where  $\rho(x_0, y_0)$  is the reflectivity of the point scatterer.

If point scatterer has only a translational motion with a velocity of  $v_r$ , at time  $t$ , the range becomes,

$$r(t) = r_0 + v_r t \quad (2.10)$$

If the point scatterer only has a rotational motion with angular rotation rate of  $\Omega$ , the range at time  $t$  becomes,

$$r(t) = (R_0^2 + d_0^2 + 2d_0R_0 \sin(\Theta_t))^{1/2} \quad (2.11)$$

Assuming  $R_0 \gg d_0$ , Equation (2.11) can be rewritten as [1]

$$r(t) = R_0 + x_0 \sin(\Omega t) + y_0 \cos(\Omega t) \quad (2.12)$$

Therefore, range of the point scatterer with complex motion becomes,

$$r(t) = R_0 + v_r t + x_0 \sin(\Omega t) + y_0 \cos(\Omega t) \quad (2.13)$$

Hence, return signal from the entire target can be represented by integrating the differential point scatterer response over the entire spatial domain, [14]

$$\begin{aligned} S(f, t) &= \int_{-\infty}^{\infty} \int_{-\infty}^{\infty} \rho(x, y) \exp(-j2\pi f \frac{2(R_0 + v_r t + x_0 \sin(\Omega t) + y_0 \cos(\Omega t))}{c}) dx dy \\ &= \exp(-j2\pi f \frac{2(R_0 + v_r t)}{c}) \int_{-\infty}^{\infty} \int_{-\infty}^{\infty} \rho(x, y) \exp(-j2\pi f \frac{2(x_0 \sin(\Omega t) + y_0 \cos(\Omega t))}{c}) dx dy \end{aligned} \quad (2.14)$$

The objective of radar image processing is to estimate the target's reflectivity density function,  $\rho(x, y)$  [1]. If the  $\exp(-j2\pi f \frac{2(R_0 + v_r t)}{c})$  term is removed,  $\rho(x, y)$  can be obtained by simply taking the inverse Fourier transform over the spatial dimensions. Removal procedure of this phase term is called gross motion compensation.

The cross-range resolution in this case can be written as [1],

$$\Delta r_{cr} = \frac{\lambda}{2\Omega T} \quad (2.15)$$

where  $T$  is the observation time.

## 2.4 Step Frequency Modulated Radar

There are several radar waveforms suitable for radar imaging, such as impulse waveform, Doppler-chirp waveform and stepped frequency waveform [15]. The simulations conducted for this study is done using stepped frequency waveform. Therefore, detailed explanation of the basic parameters of step frequency modulated radar and their relationship with radar resolution concept will be beneficial.

Step frequency modulated radar transmitted pulse waveform can be represented as,

$$s_T(t) = \cos(2\pi(f_0 + i\Delta f)t)w(t) \quad (2.16)$$

Where  $f_0$  is carrier frequency,  $\Delta f$  is frequency step size,  $i$  is the pulse index ranging from zero to number of pulses used, and window function  $w(t)$  is defined as,

$$w(t) = \begin{cases} 1, & -\frac{T}{2} \leq t \leq \frac{T}{2} \\ 0, & \text{otherwise} \end{cases} \quad (2.17)$$

The stepped frequency modulated radar transmits N bursts that are composed of M pulses over an integration time. Figure 2.4 shows the frequency of pulses on each bursts.

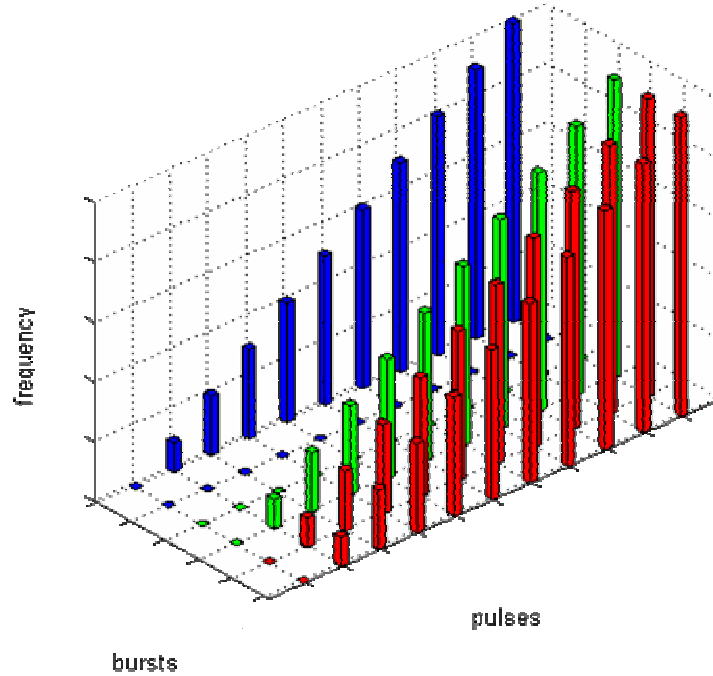


Figure 2.4: Frequency of pulses over the integration time

The bandwidth of the stepped frequency modulated radar can be derived from the explanation above. Since each frequency of each consecutive pulse in a burst is increased by an amount of  $\Delta f$ , and there are M pulses in a burst, bandwidth of the radar becomes  $\beta = M\Delta f$ . Therefore range resolution offered by a stepped frequency modulated radar is, [1]

$$\Delta r_r = \frac{c}{2M\Delta f} \quad (2.18)$$

In stepped frequency modulated radar, each consecutive pulse is transmitted after an interval, which is called Pulse Repetition Interval (PRI). Pulse Repetition Frequency (PRF) can be defined as  $PRF = 1/PRI$ . Therefore, image integration time, or observation time, can be calculated as the product of PRI, number of pulses, and number of bursts. As mentioned before, observation time directly affects the cross-range resolution. The formulation for cross-range resolution for step frequency modulated radar is  $\Delta r_{cr} = \lambda / 2\Omega MNPRI$ . Figure 2.5 illustrates the step frequency modulated inverse synthetic aperture radar imaging of a moving target.

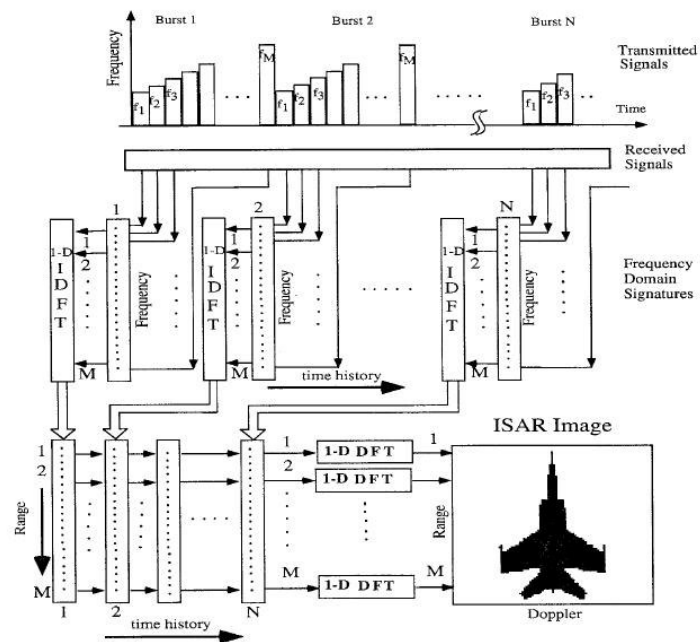


Figure 2.5: Stepped-frequency ISAR imaging of a moving target [9]

## 2.5 ISAR Data Simulation

Man-made targets have a large variety of backscattering properties. Discontinuities are scatterers whose effective extends are relatively small in terms of the wavelength so that they essentially act as fixed point scatterers. Smooth extended surfaces are flat or rounded plates on the vehicle. If the surface happens to be illuminated at its broadside aspect, it will generate a huge return. Cavity type reflectors like exhaust of an engine duct of a fighter aircraft, generates multiple delayed returns which spread in range and Doppler [16].

The target modeled with a set of point scatterers or scattering centers, described by their reflectivity and locations in the target coordinate system. The term reflectivity has been used to refer to the amplitude and phase of the echo response at a given viewing angle for a given set of radar parameters. This coordinate system embedded on the target, its origin is the geometric center of the target. Although it can not represent the many real life situations, the point scatterer model is simple and helpful for studying algorithms of image formation, auto focusing, motion compensation and the effect of target motion on ISAR images. In the simulation radar is located at the origin of the Earth centre Earth fixed (ECEF) coordinate system. In other words, radar is considered stationary all the time as ISAR theory suggests. Figure 2.6 shows an aircraft model composed of point scatterers.

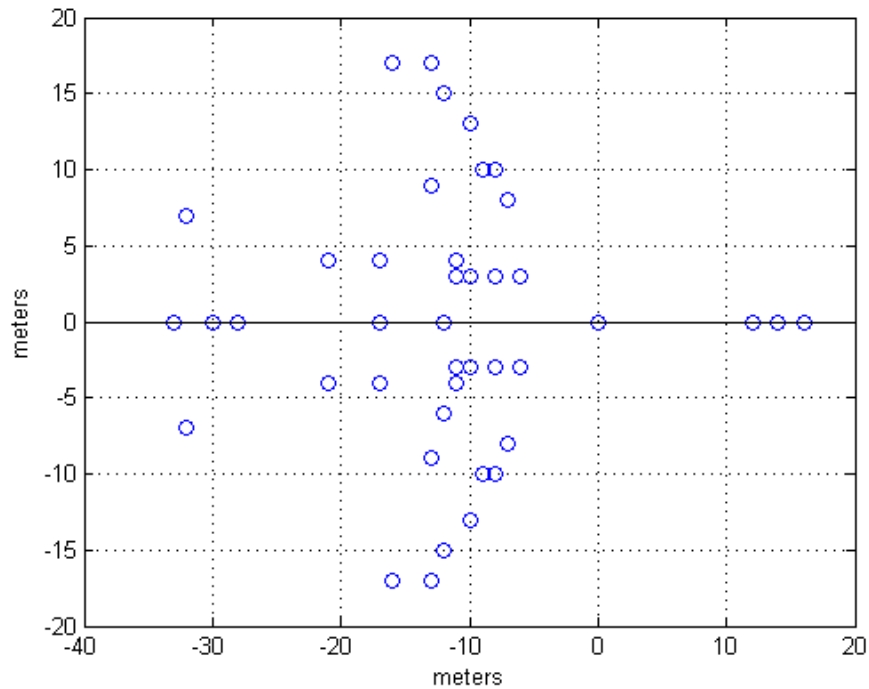


Figure 2.6: A point scatterer aircraft model

The procedure of simulation for a stepped frequency ISAR raw data generation can be summarized as follows [15];

*Step 1:* Select radar parameters (center frequency, frequency step size, PRI, number of pulses, number of bursts, etc)

*Step 2:* Select a point scatterer model for the target. (Locations of the point scatterers and their individual reflectivities)

*Step 3:* Select target motion parameters (initial position, velocity etc.)

*Step 4:* Transmit the radar signal repeatedly, update the target position, and calculate the return signal

*Step 5:* Arrange the return signals into a matrix of size number of bursts by number of pulses

*Step 6:* Perform the gross motion compensation

After gross motion compensation step, the data can be applied to the radar imaging algorithms.

## CHAPTER 3

# JOINT TIME-FREQUENCY TRANSFORMATIONS FOR RADAR IMAGING

### 3.1 Introduction

In this chapter, several joint time frequency transforms are introduced and discussed. Although it can not meet many necessities such as resolution, instantaneous frequency, etc, short time Fourier transform is examined in detail because it gives the basic understanding of joint time frequency analysis of signals. Inverse of sampled short time Fourier transform or discrete Gabor transform is discussed next. Discrete Gabor transform is one of the fundamental steps of conducting time frequency distribution series analysis of a signal, which is explained in detail in the last section of this chapter. After discrete Gabor transform, Wigner-Ville distribution is explained. Apart from time frequency distribution series, adaptive Gaussian representation is also examined in this chapter as a means of suppression of cross-term interference generated by Wigner-Ville distribution.

Each time-frequency transform is exemplified with several sample signals. Sample signal no. 1 is composed of sum of three sinusoidal functions at frequencies 1 kHz, 2 kHz and 7.7 kHz. Sample signal no. 2 is sum of sinusoidal functions like sample signal no.1. Two impulses added to this

functions at 2 msec and 4 msec. Sample signal 3 is only two impulses with hit times of 2 msec. and 3.6 msec. All the three signals have 128 samples and sampling interval for these signals is 0.04 msec. These signals are selected due to their extreme time-frequency characteristics. In addition to those three signals, sound of bat is also examined with some of the transformations explained. This signal has nonlinear frequency changes and has a sampling interval of 7 microseconds. The data is obtained from <http://www-dsp.rice.edu/software/TFA/RGK/BAT/batsig.sig>. Time plots of the sample signals and the bat signal are given in Figure 3.1 and 3.2, respectively.

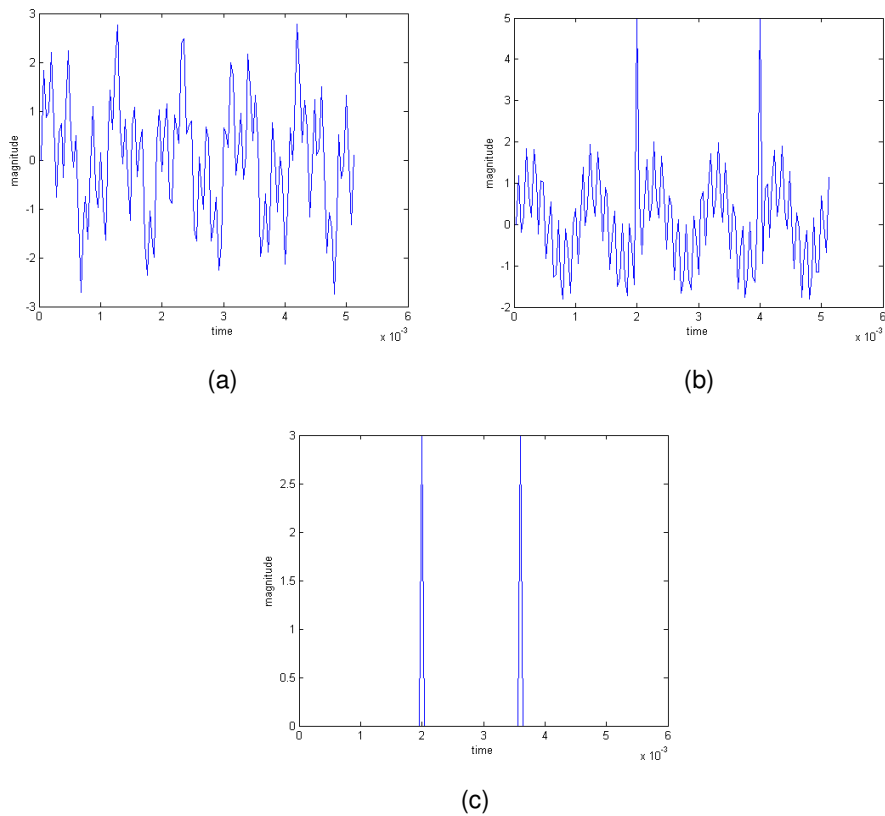


Figure 3.1: (a) Sample signal No.1 (b) Sample Signal No. 2  
(c) Sample Signal No. 3

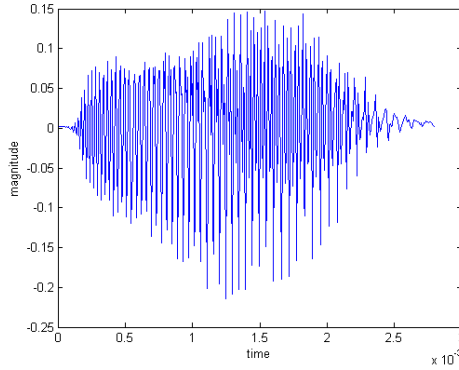


Figure 3.2: Bat Signal

### 3.2 Short Time Fourier Transform (STFT)

In regular Fourier transform, the signal under examination is compared with the complex sinusoidal functions which spread into the entire time domain and therefore not concentrated in time domain. As a result of this fact, Fourier transform does not explicitly indicates how the signal evolves in time although this information is hidden in the phase term. In order to overcome this problem, one may decide to use functions which are localized in both time and frequency domains simultaneously instead of complex sinusoidal functions. The idea can be formulated as follows; [23]

$$STFT(t, w) = \int s(\tau) \gamma_{t,w}^*(\tau) d\tau = \int s(\tau) \gamma^*(\tau - t) e^{-jw\tau} d\tau \quad (3.1)$$

There are several ways to understand the Equation (3.1). The equation formulates a regular Fourier transform of the signal  $s(\tau) \gamma^*(\tau - t)$ . Assuming the window function  $\gamma$  has a short time duration, by moving the window function and taking Fourier transforms, one can obtain a rough idea of how

the signal's frequency content changes with time. The Figure 3.3 depicts the idea.

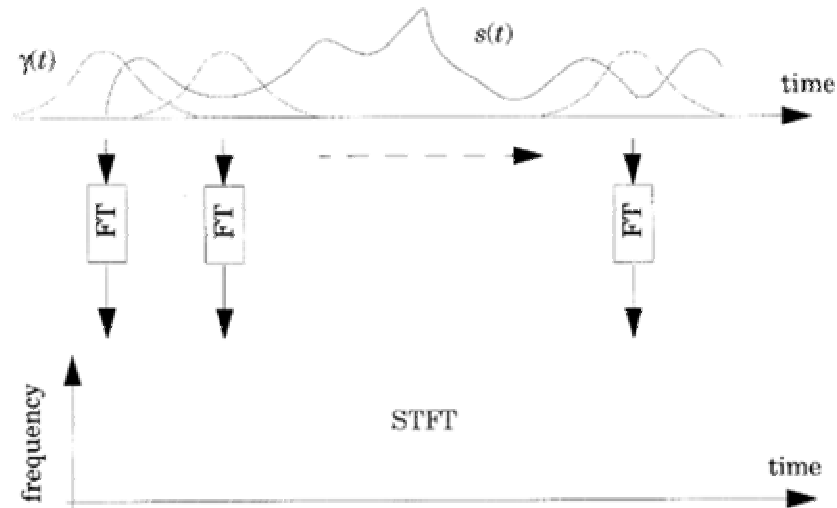


Figure 3.3: STFT operation.

Alternatively, one can interpret the equation under examination as follows; the signal  $s(\tau)$  is compared with a set of elementary functions  $\gamma^*(\tau-t)\exp\{-jw\tau\}$  that are concentrated in both time and frequency domains. Suppose that the function  $s(\tau)$  is centered at  $t=0$  and its Fourier transform is centered at  $\omega=0$ . If the time duration and frequency bandwidth of  $s(\tau)$  are  $\Delta_t$  and  $\Delta_w$  then  $STFT(t,w)$  in (3.1) indicates a signal's behavior in the vicinity of  $[t-\Delta_t, t+\Delta_t] \times [w-\Delta_w, w+\Delta_w]$  [23].

Unfortunately,  $\Delta_t$  and  $\Delta_w$  are bounded to each other by the well-known uncertainty principle [23]. That is,

$$\Delta_t \Delta_w \geq \frac{1}{2} \quad (3.2)$$

The equality holds when  $\gamma(t)$  is a Gaussian function. A function  $h(t)$  that satisfies the following differential equation also satisfies the uncertainty principle with equality [23], [28].

$$\frac{d}{dt} h(t) = -kth(t) \quad (3.3)$$

A simple solution to this differential equation is,

$$h(t) = ce^{-\frac{k}{2}t^2} \quad (3.4)$$

The window function must be of a unit norm function in order not to disturb the signal under examination. This fact injects another constraint besides uncertainty principle, which helps to find out the constant  $c$ . This constraint can be formulated as follows;

$$E_h = \int_{-\infty}^{\infty} |h(t)|^2 dt = 1 \quad (3.5)$$

Therefore, optimum window function to evaluate STFT is [28],

$$h(t) = \sqrt[4]{\frac{k}{\pi}} e^{-\frac{k}{2}t^2} \quad (3.6)$$

The square of STFT is named STFT spectrogram. It depicts a signal's energy distribution over time-frequency domain.

Synthesis problem for STFT can be analyzed as follows;

Taking the inverse Fourier transform with respect to  $STFT(t, \omega)$  in Equation (3.1) yields,

$$\begin{aligned} \frac{1}{2\pi} \int STFT(t, \omega) e^{j\mu\omega} d\omega &= \frac{1}{2\pi} \iint s(\tau) \gamma(\tau - t) e^{j(\mu - \tau)\omega} d\tau d\omega \\ &= \int s(\tau) \gamma(\tau - t) \delta(\mu - \tau) d\tau = s(\mu) \gamma(\mu - t) \end{aligned} \quad (3.7)$$

Let  $\mu = t$  then,

$$s(t) = \frac{1}{2\pi\gamma(0)} \int STFT(t, \omega) e^{j\mu\omega} d\omega \quad (3.8)$$

Which implies given  $STFT(t, \omega)$  for all  $\omega$  and  $t$  the signal  $s(t)$  can be recovered completely.

For the digital signal processing application, it is necessary to extend the STFT framework to discrete time signal. Each Fourier transform in the STFT has to be replaced by the discrete Fourier transform. The resulting STFT is discrete in both time and frequency [23].

$$STFT[k, n] = \sum_{i=0}^{L-1} s[i] \gamma[i - k] e^{-2\pi i j / L} \quad (3.9)$$

The sample signal no. 2, which is shown in Figure 3.1, is analyzed with two different window functions for the demonstration of STFT. Both

windows are same length Gaussian windows with unit energy. However, their variances are different as shown in Figure 3.4. The first window has a small variance in time domain and as a result it has a large variance in frequency domain. Therefore, STFT computed using this window is capable of resolving the time changes better. The result of the STFT analysis is shown in Figure 3.5. The impulses can be identified from the figure. The second window has large time variance, therefore its time resolution is suffering. However, unlike Figure 3.5, Figure 3.6 has good frequency resolution and two sinusoidal functions can be identified precisely.

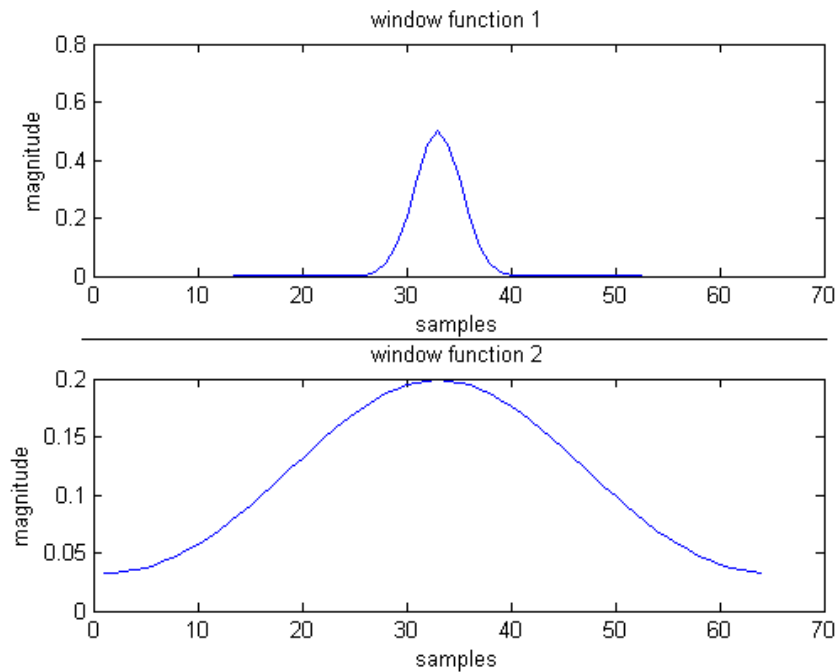


Figure 3.4: Gaussian windows used in the computation of STFT

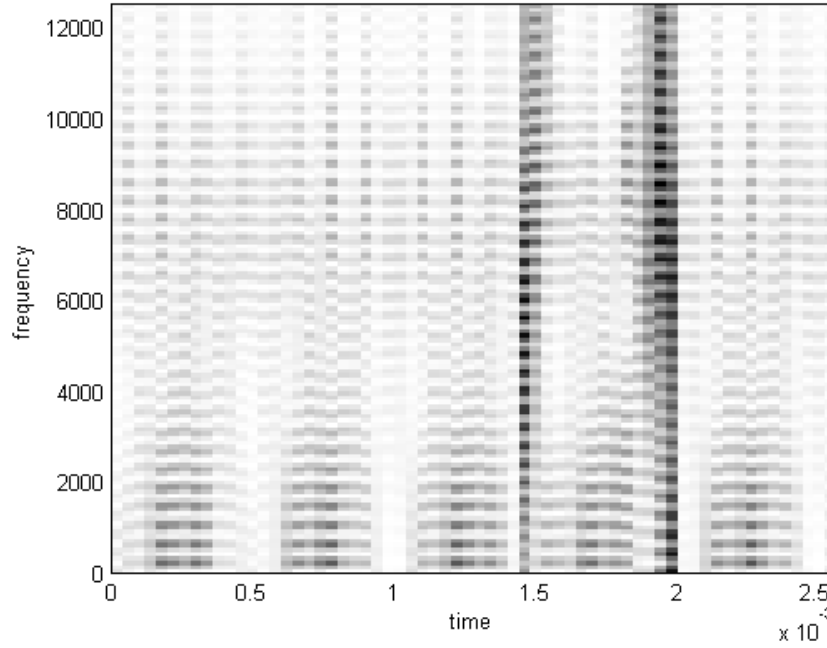


Figure 3.5: STFT of sample signal 2 with the 1<sup>st</sup> window function of Figure 3.4

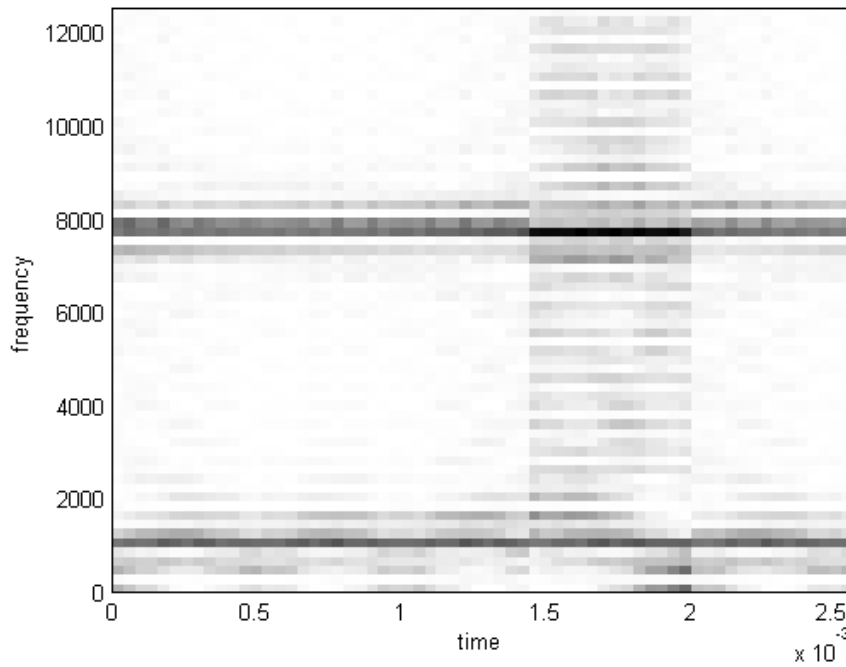


Figure 3.6: STFT of sample signal 2 with the 2<sup>nd</sup> window function of Figure 3.4

### 3.3 Discrete Gabor Transform (DGT)

In 1946, Dennis Gabor suggested to represent a signal in time-frequency plane by means of functions that occupies the smallest possible area on the plane [29]. The idea of Gabor can be formulated as follows [23]:

$$s(t) = \sum_{m=-\infty}^{\infty} \sum_{n=-\infty}^{\infty} C_{m,n} h_{m,n}(t) = \sum_{m=-\infty}^{\infty} \sum_{n=-\infty}^{\infty} C_{m,n} h(t - mT) e^{jn\Omega t} \quad (3.10)$$

where  $T$  is time-sampling interval and  $\Omega$  is frequency-sampling interval. For almost any signal  $h(t)$ , its time-shifted and frequency modulated version can be used as Gabor elementary functions. The existence condition of Equation (3.10) for arbitrary signal  $h(t)$  is [24],

$$T\Omega \leq 2\pi \quad (3.11)$$

$T\Omega = 2\pi$  is called critical sampling and  $T\Omega < 2\pi$  is called over-sampling.

If the set of Gabor elementary functions  $\{h_{m,n}\}$  is complete, there exists a dual function  $\gamma(t)$  such that the Gabor coefficients can be computed by the regular inner product rule [23]. That is,

$$C_{m,n} = \int s(t) \gamma_{m,n}^*(t) dt = \int s(t) \gamma^*(t - mT) e^{-jn\Omega t} dt = STFT(mT, n\Omega) \quad (3.12)$$

As it can be seen from Equation (3.12), Gabor coefficients can be computed using STFT in which dual function  $\gamma(t)$  used as window. Hence, discrete Gabor expansion is also named as inverse sampled STFT. However there are several difficulties related with the computation and the

time-frequency localization of the dual function. Although for continuous time STFT analysis and synthesis functions are same, it is not the case for sampled STFT representation. Unfortunately, Balian-Low theorem states that  $h_{m,n}(t)$  do not form an orthogonal basis unless  $h(t)$  is badly localized in time or frequency [1]. This means, unlike Fourier transform, dual function  $\gamma(t)$  is not equal to  $h(t)$ . Therefore,  $\gamma(t)$  is not necessarily localized both in time and frequency as  $h(t)$ . As a consequence, Gabor coefficients  $C_{m,n}$  may not reflect the local behavior of the signal [23]. Figure 3.7 shows a window and its dual function at critical sampling. Although the window is concentrated in frequency and in time, its dual is concentrated neither in time nor in frequency.

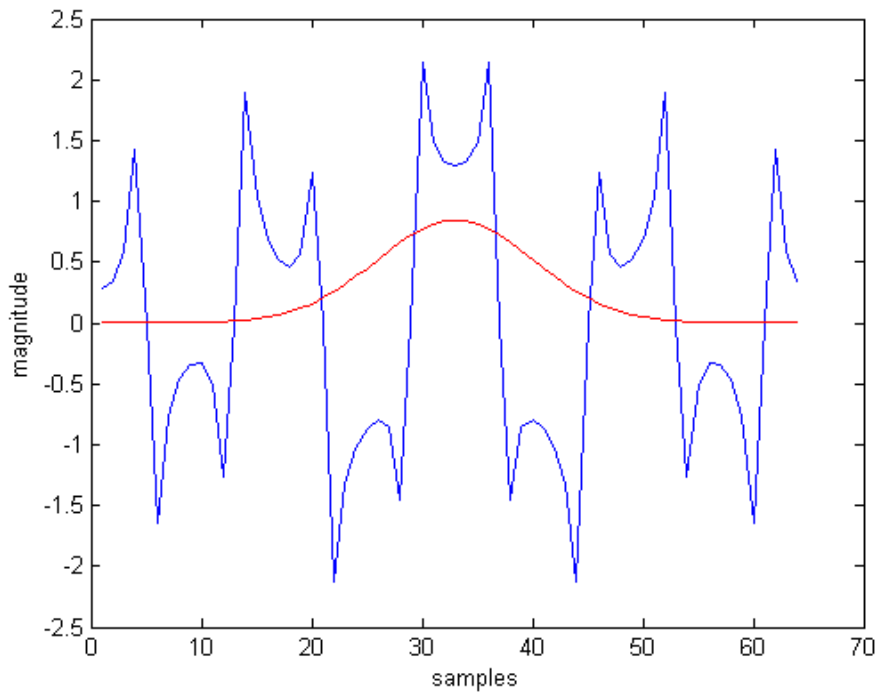


Figure 3.7: Gaussian type curve is the analysis window. The other is its dual at the critical sampling.

Several methodologies were developed to implement discrete Gabor expansion, such as filter bank methods [20], Zak-transform based methodologies [21], [22], pseudo-frame approach [23] and the approach introduced by Bastiaans [24], [25] which is expanded by Wexler and Raz [26] and later by Qian and Chen [24] Following treatment explains the last methodology mentioned above.

Substituting Equation (3.12) into right side of the Equation (3.10) yields,

$$s(t) = \int s(t') \sum_{m=-\infty}^{\infty} \sum_{n=-\infty}^{\infty} \gamma_{m,n}^*(t') h_{m,n}(t) dt' \quad (3.13)$$

In order to satisfy the Equation (3.13), the following equality must hold.

$$\sum_{m=-\infty}^{\infty} \sum_{n=-\infty}^{\infty} \gamma_{m,n}^*(t') h_{m,n}(t) = \delta(t - t') \quad (3.14)$$

Applying Poisson-sum formula, the Equation (3.14) is reduced to single integration which is called Wexler-Raz identity [26].

$$\frac{T_0 \Omega_0}{2\pi} \int h(t) \gamma(t - mT_0) e^{jn\Omega_0} dt = \delta(m) \delta(n) \quad (3.15)$$

where  $T_0 = 2\pi/\Omega$  and  $\Omega_0 = 2\pi/T$

For periodic discrete time signals, Gabor expansion can be defined by sampling the Equations (3.10) and (3.12) [23]

$$\tilde{s}[k] = \sum_{m=0}^{M-1} \sum_{n=0}^{N-1} \tilde{C}_{m,n} \tilde{h}[k - m\Delta M] e^{2\pi n \Delta N k / L} \quad (3.16)$$

$$\tilde{C}_{m,n} = \sum \tilde{s}[k] \tilde{\gamma}[k - m\Delta M] e^{-2\pi n \Delta N k / L} \quad (3.17)$$

Applying a similar procedure as done in the continuous case and applying discrete Poisson-sum formula one may obtain the discrete version of Wexler-Raz identity or the discrete version of Equation (3.15) [23], [26],

$$\sum_{k=0}^{L-1} \tilde{h}[i + mN] e^{-2\pi n i / \Delta M} \tilde{\gamma}^*[i] = \frac{\Delta M}{N} \delta[m] \delta[n] \quad (3.18)$$

where  $0 \leq n < \Delta M$  and  $0 \leq m < \Delta N$ . The equation can be rewritten in the matrix form as following,

$$\begin{aligned} H_{p \times L} \gamma_{L \times 1}^* &= \mu_{p \times 1} \\ \mu_{p \times 1} &= (1, 0, 0, \dots, 0)^T \end{aligned} \quad (3.19)$$

where  $p = \Delta M \Delta N$  and the matrix entries are generated by

$$\begin{aligned} H(m\Delta M + n, i) &= \tilde{h}[i + mN] e^{-2\pi n M i / L} \\ 0 \leq m < \Delta N, 0 \leq n < \Delta M, 0 \leq i < L \end{aligned} \quad (3.20)$$

For critical sampling, solution of Equation (3.19) is unique if matrix  $H$  is nonsingular and as stated before it is not concentrated in both frequency and time domains. However, at oversampling the system is underdetermined and there exists more than one solution for  $\gamma(t)$  [24]. One can impose additional constraint for the selection of dual functions produced by the underdetermined system as follows [26], [24].

$$\Gamma = \min_{\tilde{\gamma}: H\tilde{\gamma}^* = \mu} \left\| \frac{\tilde{\gamma}[i]}{\|\tilde{\gamma}[i]\|} - \tilde{h}[i] \right\|^2 \quad (3.21)$$

Above constraint dictates a selection of a normalized  $\gamma(t)$  which is most similar to  $h[i]$ . Since,  $h[i]$  is expected to be localized in time and frequency, the function  $\gamma(t)$  which is most similar to  $h[i]$  is also localized and therefore Gabor coefficients reflects the local behavior of the signal. In [24], the dual function selected in this manner is called  $\gamma(t)_{opt}$  and the resulting representation of the signal by Gabor coefficients is called orthogonal-like Gabor representation.

The detailed treatment to Equation (3.21) can be found at [26] and [24]. If matrix H is full row rank, resulting equation is [24],

$$\gamma_{opt}^* = H^T (HH^T)^{-1} \mu \quad (3.22)$$

which is the pseudo-inverse of matrix H.

Once optimum dual function is found, it is rather trivial to compute the Gabor coefficients using Equation (3.12). Details of this computation can be found at [23], [24].

Figure 3.8 (a) shows an analysis function with length of 128 samples that is used in periodic Gabor expansion. Figure 3.8 (b) shows the dual of the function generated with intent to analyze a function of same length using periodic discrete Gabor expansion. The time sampling step is 16 and dual generated with critical sampling. It is clear from the figure that the dual function is not concentrated in time and frequency domains. Therefore,

Gabor coefficients of sample signal no. 2, which are the sampled STFT of the signal using the dual function as window, does not represent the signals local behavior as shown in Figure 3.8 (c). However, reconstruction using the Gabor coefficients is successful with a reconstruction error of  $2.312 \cdot 10^{-16}$ .

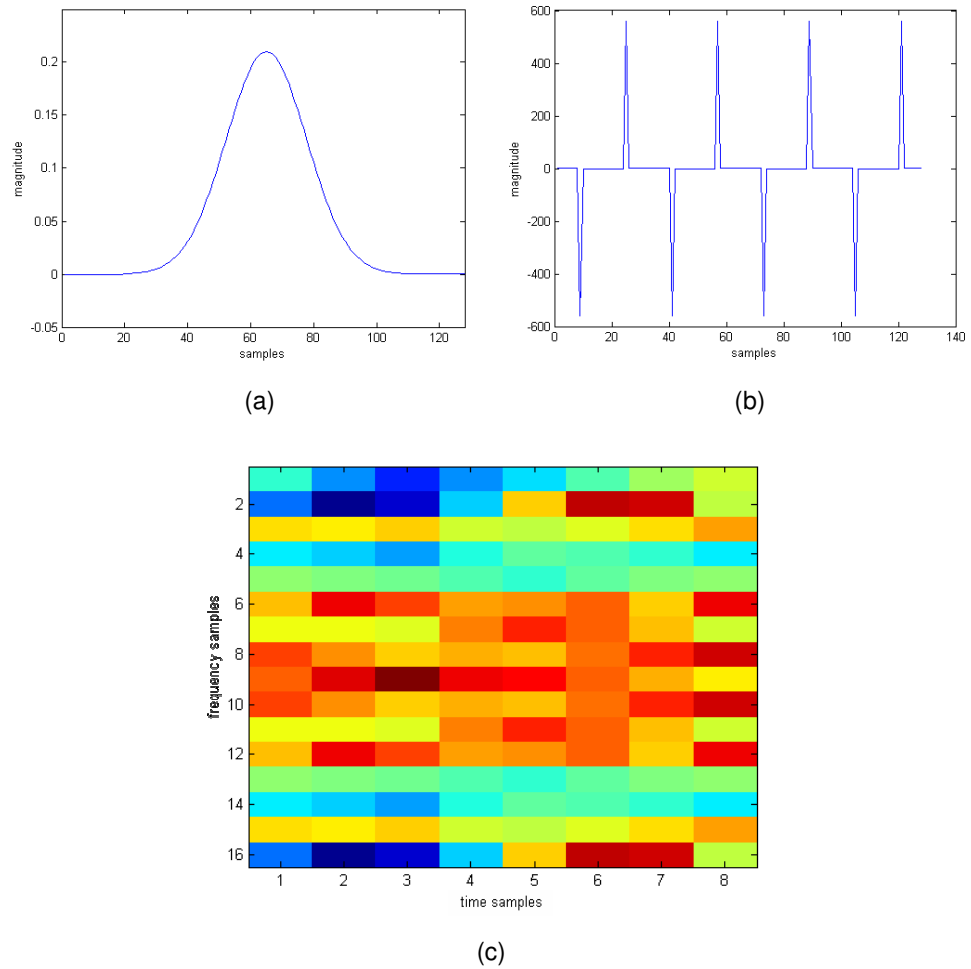


Figure 3.8: Periodic discrete Gabor analysis of sample signal no. 2 of Figure 3.1(b) at critical sampling, (a) analysis function, (b) dual function, (c) Gabor coefficients.

The same configuration as in the above example evaluated again with only change in oversampling ratio. Dual function for the same Gaussian analysis function is computed with doubling the number of the frequency bins. Figure 3.9 (a) shows the dual function in this case. This time the dual function is localized and as a result the sinusoidal terms and impulses can be identified at Figure 3.9 (b).

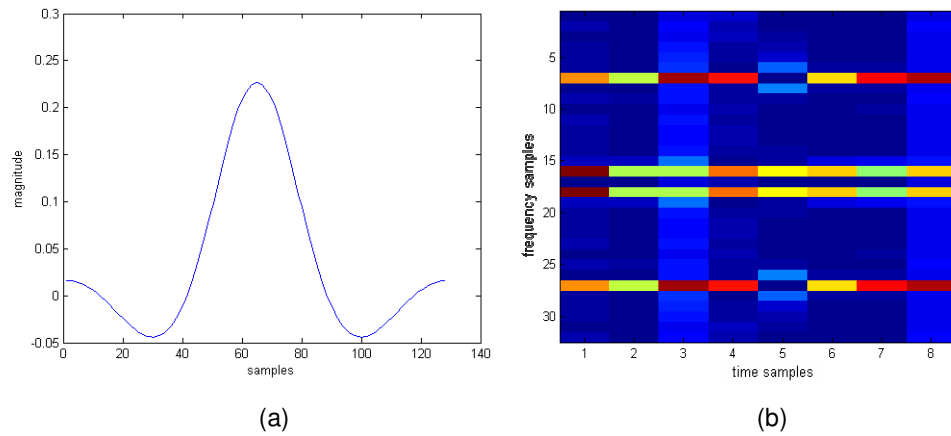


Figure 3.9: Periodic discrete Gabor analysis of sample signal no. 2 of Figure 3.1(b) at double oversampling (a) dual function, (b) Gabor coefficients.

When the same analysis carried for quadruple oversampling, the dual function and analysis function becomes nearly identical. The norm of their differences becomes as small as 0.0044. Since the time sampling steps kept constant, this refinement affects the frequency resolution. Figure 3.10 (a) and (b) shows the results for the quadruple oversampling case.

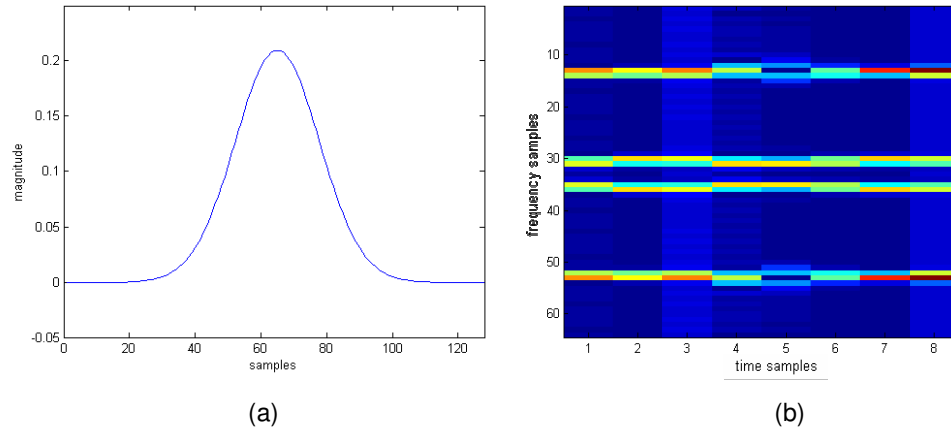


Figure 3.10: Periodic discrete Gabor analysis of sample signal no. 2 of Figure 3.1(b) at quadruple oversampling (a) dual function, (b) Gabor coefficients.

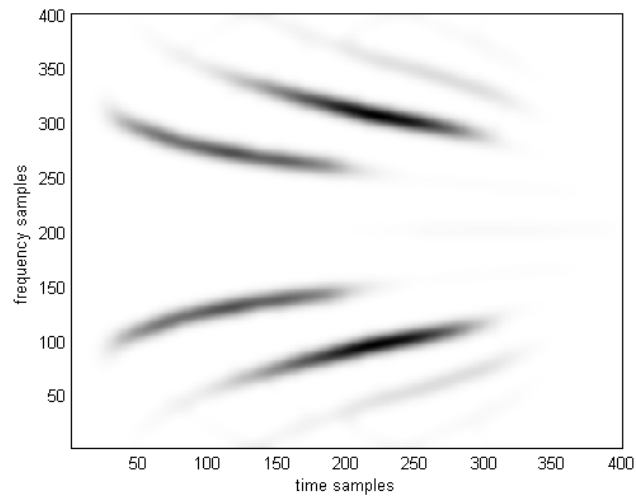


Figure 3.11: Bat signal using periodic discrete Gabor expansion with full resolution

The expansion explained above is useful when analyzed signal has relatively small number of samples. Any finite signal that can be periodized is a natural candidate for periodic discrete Gabor expansion. However, there are many applications where the signal to be analyzed composed of

large number of samples. Since in periodic discrete Gabor expansion, analysis and dual functions must be of same size with the signal, it is not suitable for those signals. Following is the treatment for infinite length signal case.

Let  $s[i]$  be a finite signal with length  $L_s$  and synthesis window  $h[i]$  with length  $L$ . One can construct following periodic sequences from these signals as following [24].

$$\begin{aligned} \tilde{s}[i] = \tilde{s}[i + kL_0] &= \begin{cases} 0 & -L \leq i < 0 \\ s[i] & 0 \leq i < L_s \end{cases} \\ \tilde{h}[i] = \tilde{h}[i + kL_0] &= \begin{cases} h[i] & 0 \leq i < L \\ 0 & L \leq i < L_0 \end{cases} \\ k &= 0, \pm 1, \pm 2, \dots \end{aligned} \quad (3.23)$$

These sequences are periodic with  $L_0 = L + L_s$ . One can apply the periodic discrete Gabor expansion to these sequences. Moreover, discrete Wexler-Raz identity may be directly applied to the periodized synthesis window.

$$\begin{aligned} \sum_{i=0}^{L_0-1} \tilde{h}[i + mN] e^{-2\pi ni / \Delta M} \tilde{\gamma}^*[i] &= \delta[m] \delta[n] \\ 0 \leq m < \frac{L_0}{N} \text{ and } 0 \leq n < \Delta M & \end{aligned} \quad (3.24)$$

If  $\tilde{\gamma}[i]$  is defined as

$$\begin{aligned} \tilde{\gamma}[i] = \tilde{\gamma}[i + kL_0] &= \begin{cases} \gamma[i] & 0 \leq i < L \\ 0 & L \leq i < L_0 \end{cases} \\ k &= 0, \pm 1, \pm 2, \dots \end{aligned} \quad (3.25)$$

then the Equation (3.24) can be rewritten as [24]

$$\sum_{i=0}^{L-1} \bar{h}[i + mN] e^{-2\pi ni / \Delta M} \gamma^*[i] = \delta[m] \delta[n] \quad (3.26)$$

$$0 \leq m < \frac{2L}{N} - 1 \text{ and } 0 \leq n < \Delta M$$

where  $\bar{h}[i]$  is defined as

$$\bar{h}[i] = \bar{h}[i + k(2L - N)] = \begin{cases} h[i] & 0 \leq i < L \\ 0 & L \leq i < 2L - N \end{cases} \quad (3.27)$$

$$k = 0, \pm 1, \pm 2, \dots$$

After this treatment, discrete Wexler-Raz identity is completely independent from length of the analyzed signal. Again, one can write the Equation (3.26) in matrix form.

$$\bar{H} \gamma^* = \mu \quad (3.28)$$

$$\mu = (1, 0, 0, \dots, 0)^T$$

This time  $\bar{H}$  is a  $(2\Delta M / N)L - \Delta M \times L$  matrix constructed by,

$$\bar{H}(m\Delta M + n, i) = \bar{h}[i + mN] e^{-2\pi ni / \Delta M}$$

$$0 \leq m < \frac{2L}{N} - 1, 0 \leq n < \Delta M, 0 \leq i < L \quad (3.29)$$

It is worth restating that above analysis is valid only if dual function is defined as in Equation (3.25).

With  $L$  remaining finite, letting  $L_s \rightarrow \infty$  thereby  $L_0 \rightarrow \infty$ , the periodic discrete Gabor expansion defined for periodic sequences  $\tilde{s}[i]$ ,  $\tilde{h}[i]$  and

$\tilde{\gamma}[i]$  becomes discrete Gabor transform pair for infinite sequences in following form [24]. That is,

$$s[i] = \sum_{m=-L/\Delta M}^{\infty} \sum_{n=0}^{N-1} C_{m,n} h[i - m\Delta M] e^{2\pi n i / N} \quad (3.30)$$

$$C_{m,n} = \sum_{i=0}^{\infty} s[i] \gamma^*[i - m\Delta M] e^{2\pi n i / N} \quad (3.31)$$

Equation (3.31) is called discrete Gabor Transform and Equation (3.30) is called inverse discrete Gabor transform.

Similar to the periodic case, oversampled DGT has an orthogonal-like representation. The dual function that should be used in order to obtain this representation is [27],

$$\gamma_{opt}^* = \bar{H}^T (\bar{H}\bar{H}^T)^{-1} \bar{\mu} \quad (3.32)$$

The dual functions of two different types of signals are computed at different oversampling rates and the results are presented in Figure 3.12 and 3.13. At Figure 3.12 (a), the double oversampling rate is used and the error (defined as the norm of the difference of the function and dual) between the function and its dual is computed as 0.1553. When the oversampling rate is 4, the function and the dual are visually identical (see Figure 3.12 (b)). The error between these two functions is calculated as 0.0037. Figure 3.13 shows the results for a chirp-like signal to demonstrate the algorithm presented can be applied to signals other than Gaussians. Again, for quadruple oversampling, function and its dual are nearly identical. The error value for double oversampling is 0.32 while for quadruple oversampling it is 0.0103. Once the dual function is determined, computation of the Gabor coefficients is exactly the same as in the periodic Gabor expansion [24]. Therefore, no examples are given here.

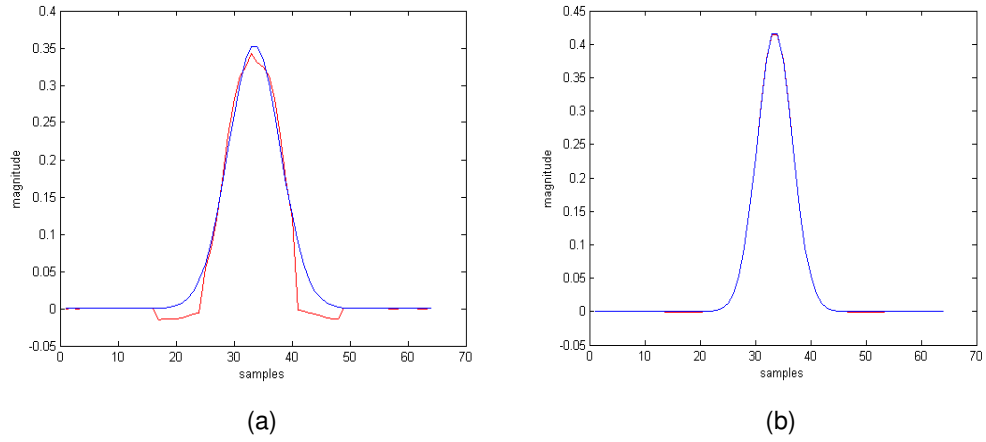


Figure 3.12: Dual functions of Gaussian type signal at (a) double and (b) quadruple sampling.

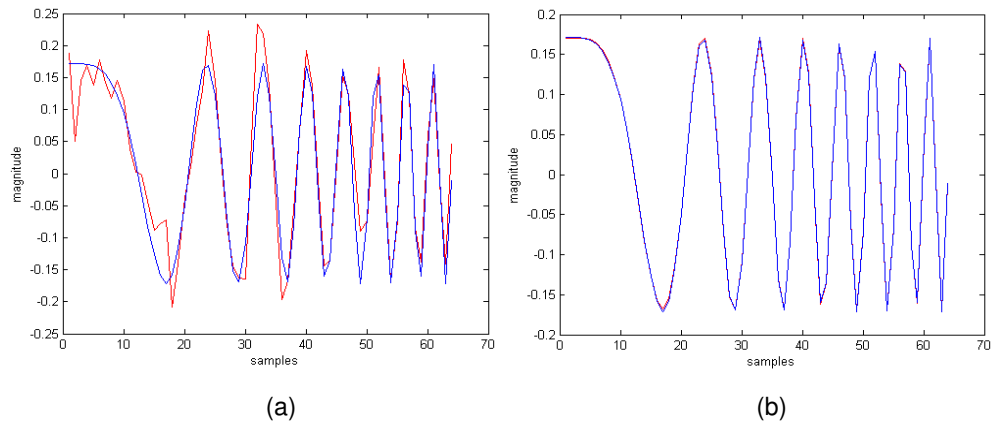


Figure 3.13: Dual functions of chirp type signal at (a) double and (b) quadruple sampling

### 3.4 Wigner – Ville Distribution (WVD)

The square of the Fourier transform is called power spectrum. Wiener - Khinchin theorem states that power spectrum can also be considered as Fourier transform of the auto-correlation function [23].

$$PS(\omega) = |S(\omega)|^2 = \int R(\tau) e^{-j\omega\tau} d\tau \quad (3.33)$$

where auto-correlation function  $R(\tau)$  is defined by,

$$R(\tau) = \int s(t) s^*(t - \tau) dt \quad (3.34)$$

This representation does not show how the signal's frequency content evolves in time. Instead of Equation (3.34), one can define a time dependent auto-correlation function in order to obtain a power spectrum which is time dependent. That is,

$$P(t, \omega) = \int R(t, \tau) e^{-j\omega\tau} d\tau \quad (3.35)$$

In Wigner-Ville distribution (WVD), time dependent auto-correlation function is defined as [23], [12],

$$R(t, \tau) = s\left(t + \frac{\tau}{2}\right) s^*\left(t - \frac{\tau}{2}\right) \quad (3.36)$$

Therefore Wigner-Ville distribution is formulated as,

$$WVD(t, \omega) = \int s\left(t + \frac{\tau}{2}\right) s^*\left(t - \frac{\tau}{2}\right) e^{-j\omega\tau} d\tau \quad (3.37)$$

WVD satisfies time marginal and frequency marginal conditions. Moreover, it is a real valued function and it has instantaneous frequency property which shows the accuracy of the transform for observing the frequency content of a signal. The conditional mean frequency obtained by the WVD is equal to the mean frequency value at that time [28].

Cross-WVD is defined by using cross correlation function of the form of the Equation (3.36).

$$WVD_{s,g}(t, \omega) = \int s\left(t + \frac{\tau}{2}\right) g^*\left(t - \frac{\tau}{2}\right) e^{-j\omega\tau} d\tau \quad (3.38)$$

Although WVD possesses many useful characteristics it has a main deficiency, cross-term interference. Let the signal to be analyzed composed of two signals, i.e.  $s(t) = s_1(t) + s_2(t)$ . Using Equation (3.37),

$$WVD_s(t, \omega) = WVD_{s_1}(t, \omega) + WVD_{s_2}(t, \omega) + 2 \operatorname{Re}\{WVD_{s_1, s_2}(t, \omega)\} \quad (3.39)$$

Unfortunately, WVD of sum of signals is not equal to the sum of their respective WVDs. In fact Equation (3.39) suggests that each pair of auto-terms creates a cross-term. Cross-terms reflect the correlation of the corresponding pair of auto-terms. Its location and rate of oscillation are determined by the time and frequency centers of auto-terms [23]. Although the cross-terms has have limited contribution to properties of WVD, it often obscures time dependent spectrum patterns [14].

Sample signal no.1, which is composed of three sinusoidal functions, is examined and result is shown on Figure 3.14. At the midpoint of auto-terms oscillatory cross terms can be seen. The oscillation is in the time domain and the rate of oscillation depends on the separation of auto terms in the frequency domain.

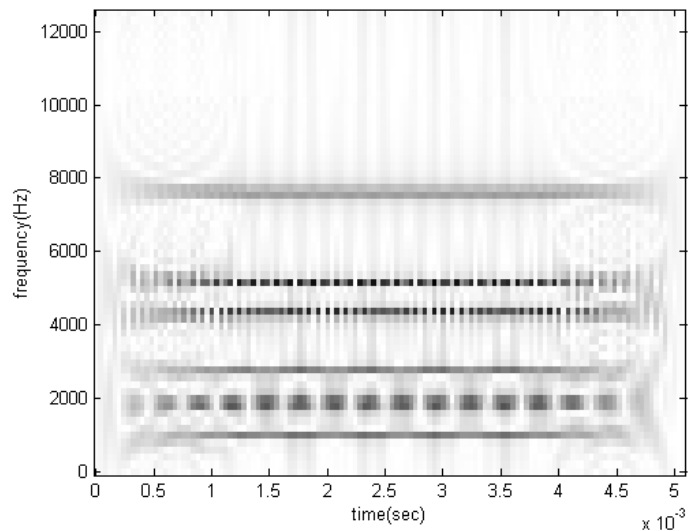


Figure 3.14: WVD of sample signal no. 1,

Sample signal no. 3 is also examined with WVD. This signal is composed of two impulses. Therefore, it occupies the entire frequency domain. At the midpoint of these impulses, cross term that oscillates in frequency can be seen at the Figure 3.15.

The last example for WVD is shown on Figure 3.16. The signal under examination is the bat signal which is evaluated before using discrete

Gabor transform at Figure 3.11. The development in the resolution in both time and frequency domains is obvious. However, cross term interface makes the auto terms completely unidentifiable.

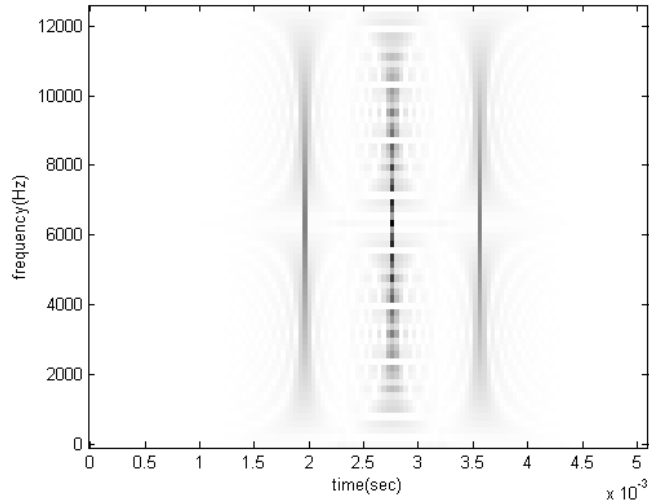


Figure 3.15: WVD of sample signal no. 3

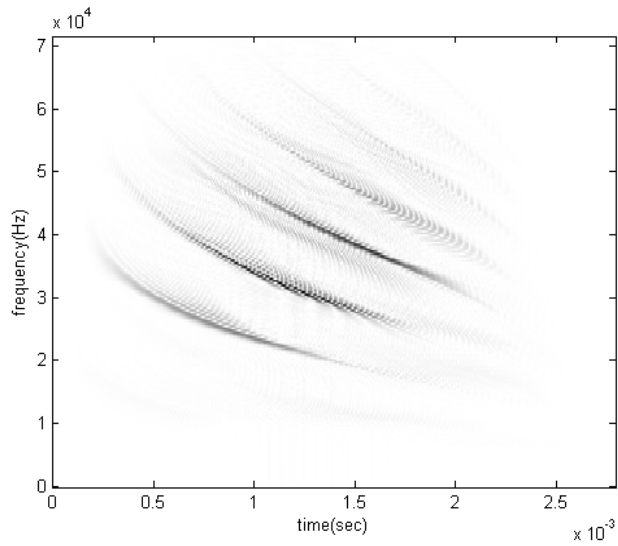


Figure 3.16: WVD of bat signal

The methods developed to reduce cross-term interference will be discussed next.

### 3.5 Adaptive Gaussian Representation (AGR)

One of the methods for suppressing cross-term interference in WVD is adaptive representation of the signal. Adaptive signal expansion is defined as [23],

$$s(t) = \sum_p B_p h_p(t) \quad (3.40)$$

Constant  $B_p$  shows the similarity between the elementary function  $h_p(t)$  and the signal  $s(t)$  and can be calculated using regular inner product.

$$B_p = \langle s(t), h_p(t) \rangle \quad (3.41)$$

The procedure of computing adaptive signal expansion is as follows:

*Step 1:* Set  $p = 0$  and  $s_0(t) = s(t)$  Then find an elementary function among the set of possibilities that maximizes  $B_p$  in the sense of,

$$|B_p|^2 = \max_{h_p} |\langle s_p(t), h_p(t) \rangle|^2 \quad (3.42)$$

Step 2: Compute the residual by,

$$s_{p+1}(t) = s_p(t) - B_p h_p(t) \quad (3.43)$$

If the energy of the elementary signal is taken as unity, the energy of the residual signal is,

$$\|s_{p+1}(t)\|^2 = \|s_p(t)\|^2 - |B_p|^2 \quad (3.44)$$

Step 3: Increase  $p$  by one and repeat Step 1 and Step 2.

These steps summarized in Figure 3.17.

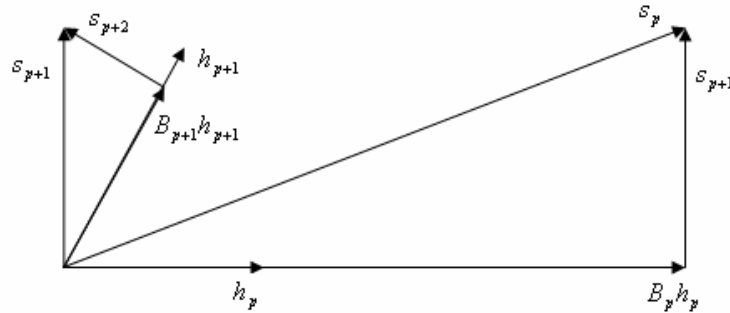


Figure 3.17: Computation procedure of adaptive representation.

The energy of the residual signal converges to zero as number of iterations increases provided that there exists an elementary function that is not orthogonal to the residual signal [11]. In other words, signal  $s(t)$  can

be represented exactly by using infinite number of elementary functions [28]. This suggests that the energy of the signal can also be computed using,

$$\|s(t)\|^2 = \sum_{p=0}^{\infty} |B_p|^2 \quad (3.45)$$

The main task of the adaptive signal representation is to find a set of elementary functions  $\{h_p(t)\}$ , that most resemble the signal's time-frequency structures and at the same time satisfy the Equations (3.40) and (3.41) [23].

Since the elementary function will contain three parameters for time center, frequency center and time width, trying to find an analytical solution for the best elementary function may not be feasible. Therefore, an iterative approach can be used for finding the best representation of the signal [11], [28], [29].

The adaptive spectrogram decomposes the signal into sum of weighted elementary functions. One may apply WVD to the decomposed signal to better control the cross terms. That is,

$$WVD_s(t, \omega) = WVD\left(\sum_p B_p h_p(t)\right) \quad (3.46)$$

Rearranging above equation yields,

$$WVD_s(t, \omega) = \sum_p B_p WVD_{h_p}(t, \omega) + \sum_{p \neq q} B_p B_q^* WVD_{h_p h_q}(t, \omega) \quad (3.47)$$

The first group represents the auto-terms and the second group represents the cross-terms [23]. WVD satisfies the time and frequency marginal conditions. So,

$$\begin{aligned}\|s(t)\|^2 &= \frac{1}{2\pi} \iint WVD_s(t, \omega) dt d\omega \\ &= \sum_p |B_p|^2 \frac{1}{2\pi} \iint WVD_{h_p}(t, \omega) dt d\omega + \frac{1}{2\pi} \iint \sum_{p \neq q} B_p B_q^* WVD_{h_p h_q}(t, \omega) dt d\omega\end{aligned}\quad (3.48)$$

If the energy of the elementary functions are selected as unity,

$$\|s(t)\|^2 = \sum_p |B_p|^2 + \frac{1}{2\pi} \iint \sum_{p \neq q} B_p B_q^* WVD_{h_p h_q}(t, \omega) dt d\omega \quad (3.49)$$

Using Equation (3.45), one can easily see that in Equation (3.49), the term corresponding to the cross-terms contains zero energy,

$$\frac{1}{2\pi} \iint \sum_{p \neq q} B_p B_q^* WVD_{h_p h_q}(t, \omega) dt d\omega = 0 \quad (3.50)$$

Therefore, a time dependent spectrum, namely Adaptive Spectrogram (AS) safely defined as,

$$AS(t, \omega) = \sum_p |B_p|^2 WVD_{h_p}(t, \omega) \quad (3.51)$$

Theoretically, the elementary functions used for the adaptive signal expansion can be very general. However, to better characterize the signal, it is desirable for the elementary functions to be localized in time and frequency simultaneously. Because the Gaussian type signal achieves lower bound of the uncertainty principle, it is a natural choice for adaptive

representation [23]. The adaptive representation that uses the Gaussian functions as elementary functions is called Adaptive Gaussian Representation [28]. So  $h_p(t)$  can be formulated as,

$$h_p(t, \omega) = \left( \frac{\alpha_p}{\pi} \right)^{1/4} e^{-\frac{\alpha_p}{2}(t-T_p)^2} e^{j\Omega_p t} \quad (3.52)$$

where  $T_p$  is the time center,  $\Omega_p$  is the frequency center and  $1/2\alpha_p$  is the variance of the Gaussian function [28].

In the adaptive representation, the variance of the elementary function is adjustable. The time and frequency centers of the elementary function are not fixed. Adjusting the variance changes the duration of the elementary function, and adjusting the parameters  $(T_p, \Omega_p)$  change the localization center. Changing the variance and the time-frequency center of the elementary function makes possible to represent the time and frequency behaviors locally.

WVD of Equation (3.52) is [23],

$$WVD_{h_p}(t, \omega) = 2 \exp \left\{ - \left[ \alpha_p (t - T_p)^2 + \frac{(\omega - \Omega_p)^2}{\alpha_p} \right] \right\} \quad (3.53)$$

Therefore, adaptive spectrogram becomes,

$$AS(t, \omega) = 2 \sum_p |B_p|^2 \exp \left\{ - \left[ \alpha_p (t - T_p)^2 + \frac{(\omega - \Omega_p)^2}{\alpha_p} \right] \right\} \quad (3.54)$$

Determination of the time center, frequency center and the variance parameters in an optimum manner is the main problem of adaptive Gaussian representation. There are several solutions to this problem. Coarse to fine search [11], matching pursuit algorithm [29], hybrid matching pursuit algorithm [28] can be listed. In this study only matching pursuit algorithm is examined. The details of the other algorithms and their comparison can be found at [28].

The maximization problem given in Equation (3.42) can be restated for Gaussian type elementary functions as following.

$$|B_\rho|^2 = \max_{T_\rho, \Omega_\rho, \alpha_\rho} |\langle s_\rho(t), h_\rho(t) \rangle|^2 \quad (3.55)$$

Instead of finding an analytical solution, the coarse to fine search algorithm tries to find the three variables that satisfies the Equation (3.55) in an iterative manner [11]. Expanding the inner product in the Equation (2.55) yields,

$$\begin{aligned} \Gamma_{T_\rho, \Omega_\rho, \alpha_\rho} &= \int s_\rho(t) h_\rho(t) dt \\ &= \left( \frac{\alpha_\rho}{\pi} \right)^{1/4} \int s_\rho(t) e^{-\frac{\alpha_\rho}{2}(t-T_\rho)^2} e^{j\Omega_\rho t} dt \end{aligned} \quad (3.56)$$

Since the above equation is nothing but the Fourier transform of  $s_\rho(t) e^{-\frac{\alpha_\rho}{2}(t-T_\rho)^2}$ , once the parameters  $\alpha_\rho$  and  $T_\rho$  are selected, the third parameter  $\Omega_\rho$  can be found as the frequency that contains largest Fourier transform coefficient.

The steps used in finding optimal parameters given below,

Step 1: Select  $\alpha_p$  in a predetermined manner.

Step 2: Change  $T_p$  throughout the signal and compute the Fourier transform of the product  $s_p(t) \exp\left\{\frac{-\alpha_p}{2}(t - T_p)^2\right\}$  until finding the largest magnitude Fourier transform coefficient.

Step 3: Repeat steps 1 and 2.

Once the elementary function which is most similar to the signal is found, coefficient  $B_p$  and remainder signal can be found and the procedure of computing adaptive spectrogram is iterated until the energy of the remainder signal is smaller than a predetermined limit.

In the simulations, selection policy used for determining  $\alpha_p$  can be described as follows.  $\alpha_p$  is selected so that variance of the elementary function is equal to the duration of the residual signal and at each iteration step,  $\alpha_p$  value is increased to decrease the variance of the function to the half of the previous value. The iterations stopped when the energy of the remainder signal becomes smaller than 1% of the original signal [28]. The resulting two-sided adaptive spectrograms for sample signals no. 1, no. 2 and no.3 and for bat signal are given in Figure 3.18. They have no cross-term interference and good resolution. However, Figure 3.18 (c), which shows the AGR of the sample signal no. 3, has an interesting interference in between the pulses. While searching for elementary function, a large variance Gaussian which covers both impulses is considered as a best fit elementary function. Therefore those elementary functions are seen on the adaptive representation. If the search procedure starts with a larger

$\alpha_p$  value, those interferences become weaker. The Figure 3.18 (d) simulates another extreme scenario for adaptive Gaussian representation. The frequency change in the signal can not be represented properly with the frequency modulated Gaussian elementary functions. One way to solve this problem is adding another parameter to elementary function to control the frequency change rate. However, no practical optimization methodology to compute the parameters is presented [23].

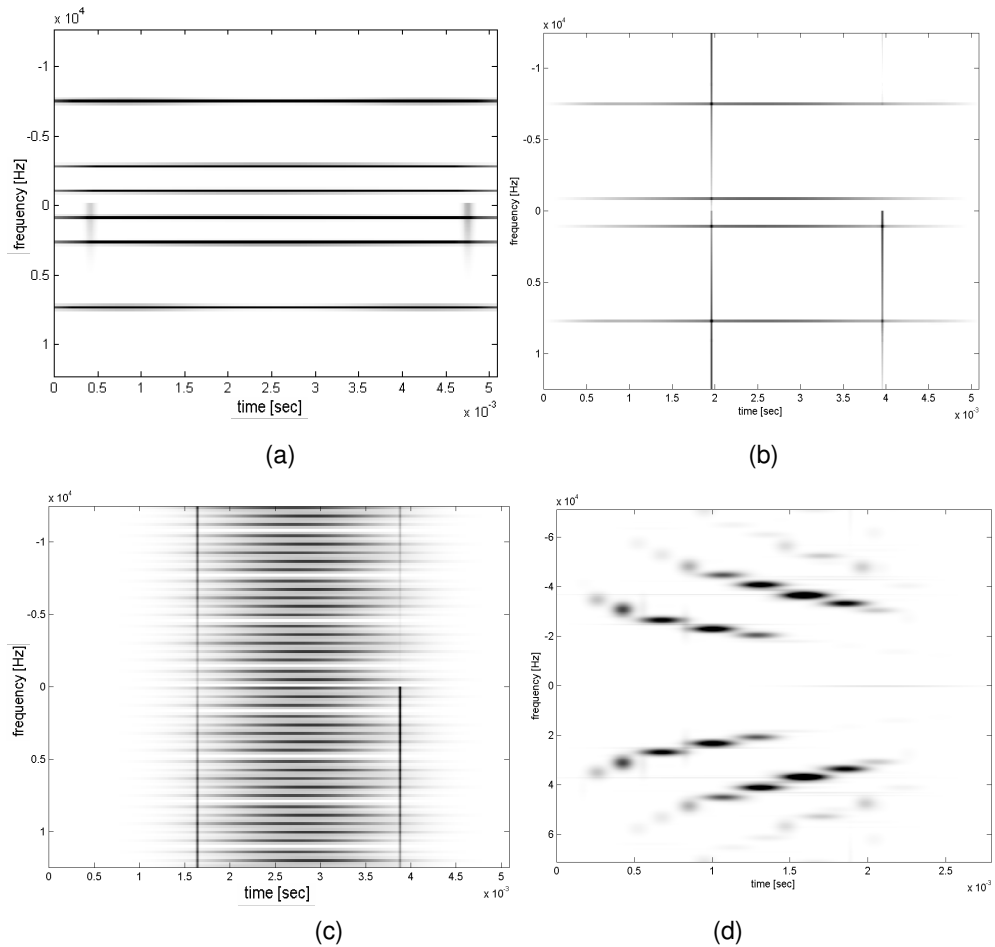


Figure 3.18: (a), (b), (c), (d) are AGR of sample signals no.1, no.2, no.3 and bat signal respectively

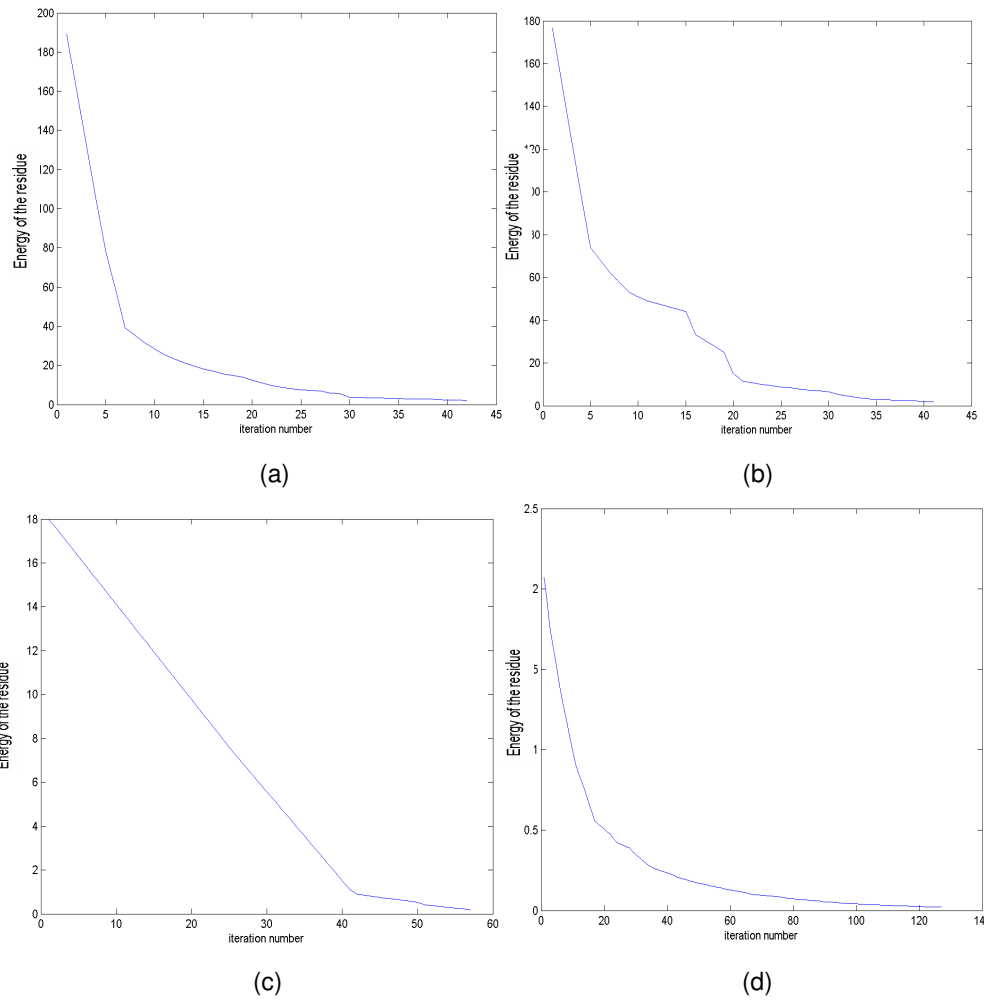


Figure 3.19: Convergence graphics for (a) sample signal no.1 (b) sample signal no. 2 (c) sample signal no. 3 and (d) bat signal

### 3.6 Time Frequency Distribution Series (TFDS)

If the WVD of a signal can be decomposed into a sum of localized and symmetric functions, it may be possible to suppress cross-term interference by selecting only the low-order harmonics [1]. This decomposition can be achieved using discrete Gabor transformation. The elementary functions used in the Gabor expansion are time and frequency shifted Gaussian functions [12]. From a theoretical point of view, two dimensional form of discrete Gabor transform is very suitable. However, there are several drawbacks such as computational expense, difficulty of the generation of the two dimensional dual function and requirement of knowing the WVD of the signal in advance [23]. Therefore, a natural choice would be one dimensional discrete Gabor transformation. The signal to be analyzed can be decomposed using 1D-DGT using Equation (3.10),

$$s(t) = \sum_{m=-\infty}^{\infty} \sum_{n=-\infty}^{\infty} C_{m,n} h_{m,n}(t) \quad (3.57)$$

$$C_{m,n} = \int s(t) \gamma_{m,n}^*(t) dt = \int s(t) \gamma^*(t - mT) e^{-jn\Omega t} dt = STFT(mT, n\Omega) \quad (3.58)$$

As discussed in chapter 2.3, orthogonal-like decomposition ensures that Gabor coefficients reflect the signal's local behavior. Taking the WVD of both sides of Equation (3.57) yields,

$$WVD_s(t, \omega) = \sum_{m,n} \sum_{m',n'} C_{m,n} C_{m',n'}^* WVD_{h,h'}(t, \omega) \quad (3.59)$$

where,

$$\begin{aligned}
WVD_{h,h'}(t,\omega) = & 2 \exp\left\{-\alpha\left(t - \frac{m+m'}{2}T\right)^2 - \frac{1}{\alpha}\left(\omega - \frac{n+n'}{2}\Omega\right)^2\right\} \\
& \exp\left\{-j\frac{n+n'}{2}\Omega(m-m')T\right\} \exp\left\{j[(m-m')T\omega + (n-n')\Omega t]\right\}
\end{aligned} \tag{3.60}$$

Taking a closer look to Equation (3.59) will be beneficial. Equation (3.59) says that WVD is composed of localized and symmetric elementary functions of the form of Equation (3.60). Those elementary functions has two dimensional Gaussian envelope located in the midpoint of the time and frequency centers of  $h(t)$  and  $h'(t)$  which is  $\frac{m+m'}{2}T$  in time and  $\frac{n+n'}{2}\Omega$  in frequency. They oscillate in time and frequency in a rate which is determined by difference of the time and frequency centers of  $h(t)$  and  $h'(t)$ . That is, WVD cross-terms oscillates in a rate of  $(m-m')T$  in time and  $(n-n')\Omega$  in frequency Based on this analysis, Time Frequency Distribution Series (TFDS) is defined as

$$TFDS_D(t,\omega) = \sum_{d=0}^D P_d(t,\omega) \tag{3.61}$$

where  $P_d(t,\omega)$  is the set of those  $WVD_{h,h'}(t,\omega)$  which have a similar contribution to the useful properties and similar influence to the cross-term. Because the impact to the cross term and as well as the useful properties are determined by the harmonic frequencies,  $(m-m')T$  and  $(n-n')\Omega$ ,  $P_d(t,\omega)$  can be considered as a set of  $WVD_{h,h'}(t,\omega)$  in which  $|m-m'| + |n-n'| = d$ . In other words, including the cross-terms around the auto-terms with a Manhattan distance of  $d$  can control the cross-term contribution to the useful properties [23]. Therefore,  $P_d(t,\omega)$  is,

$$P_d(t, \omega) = \sum_{|m-n|+|n-n'|=d} C_{m,n} C_{m',n'}^* WVD_{h,h'}(t, \omega) \quad (3.62)$$

For  $d = 0$ ,  $P_0(t, \omega)$  is a two dimensional linear time and frequency invariant interpolation filter in the form of Equation (3.63). The filter input  $|C_{m,n}|^2$  is a sampled spectrogram using a Gaussian function. The filter impulse response is a two dimensional localized Gaussian function, which is low-pass and time and frequency invariant. Hence,  $TFDS_0(t, \omega) = P_0(t, \omega)$  is similar to the STFT spectrogram [12]. As  $D$  goes to the infinity, TFDS converges to the WVD.

$$TFDS_0(t, \omega) = P_0(t, \omega) = 2 \sum_{mn=-\infty}^{\infty} |C_{m,n}|^2 \exp \left\{ -\alpha(t - mT)^2 - \frac{1}{\alpha}(\omega - n\Omega)^2 \right\} \quad (3.63)$$

Discrete formulation for the TFDS is nothing but a sampling process if the signal under examination is band limited [23].

$$DTFDS[i, k] \equiv TFDS_D(t, \omega) \Big|_{t=i\Delta t, \omega=\frac{2\pi k}{L\Delta t}} \text{ for } -\frac{L}{2} \leq k < \frac{L}{2} \quad (3.64)$$

TFDS analysis is applied to all of the sample signals and the bat signal. Results show that, TFDS of order 3 or 4 gives the best results in terms of resolution and the cross-term interference.

Figure 3.20 (a) shows TFDS of order 0 for sample signal no. 1. Figure 3.20 (b) shows TFDS of order 3 for the same signal. Increasing  $D$  results in an improvement of the resolution of the representation since cross-terms with lower oscillation rates contributes the desired characteristics of

the WVD. However as the order increases, cross-terms show themselves on the plane as interference. As Figure 3.20 (c) indicates, contribution of P of order 5 contains heavy oscillatory cross term parts of WVD. Therefore, TFDS of order 5 also starts to possess those cross terms as demonstrated in Figure 3.20 (d). Although P of order 5 contains cross-terms it is still developing the resolution of auto terms unlike P of order 20 which is shown at Figure 3.20 (e). P of order 20 only contributes to the cross terms of WVD. As the order increases, TFDS approaches to the WVD. Figure 3.20 (e) demonstrates this fact using sample signal no.1. All of the cross terms generated by the auto term pairs are clearly visible at the mid-point of the auto-terms.

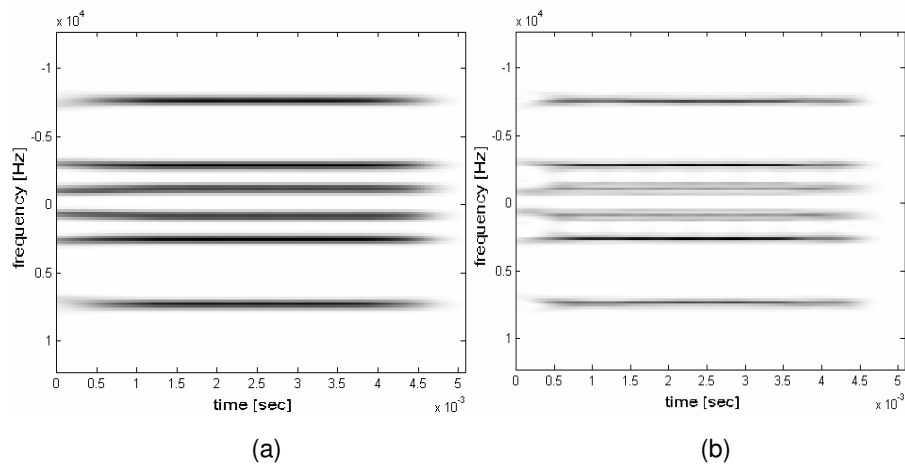


Figure 3.20: (a) TFDS of order 0, (b) TFDS of order 3

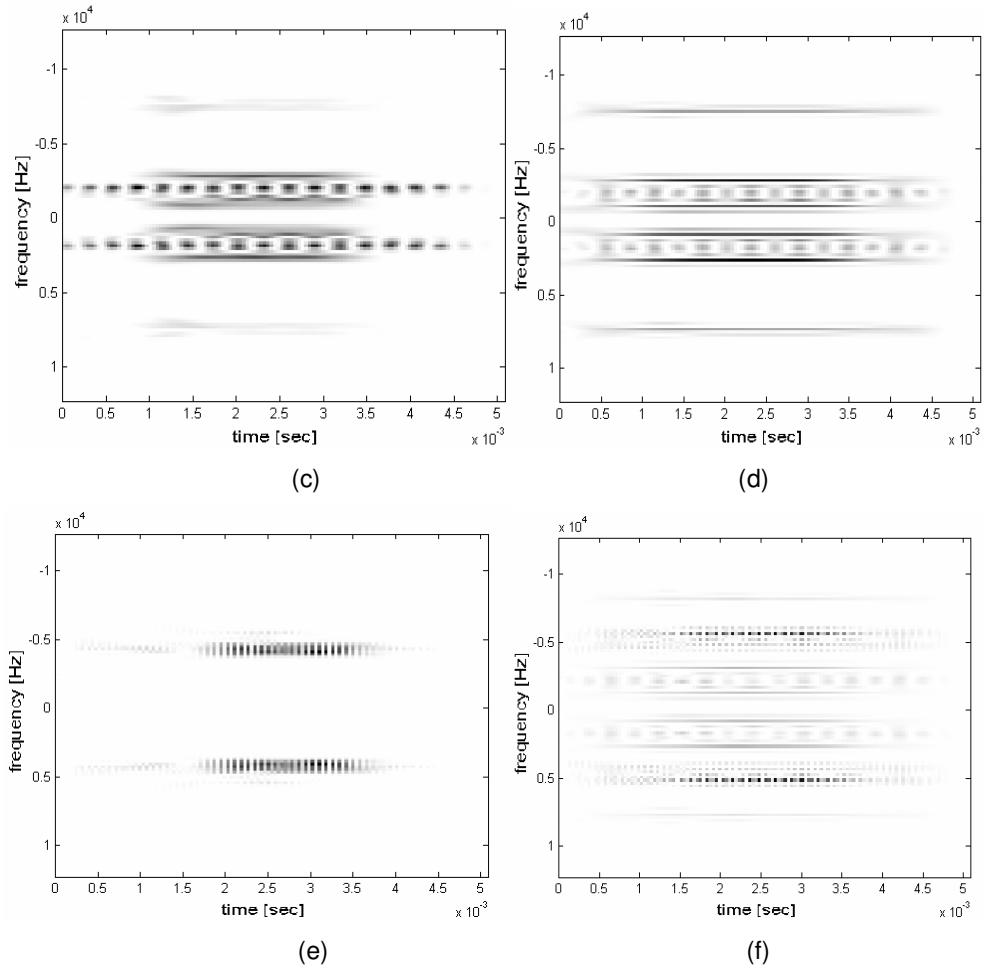


Figure 3.20 (cont'd): (c) P of order 5, (d) TFDS of order 5  
 (e) P of order 20 and (f) TFDS of order 20 for sample signal no. 1

Sample signal no. 3 contains 2 impulses, unlike sample signal no. 1 which contains 3 sinusoidal functions. Figure 3.21 contains TFDS analysis results for sample signal no. 3. Results that are similar to the results of sample signal no. 1 are obtained.

Performance of TFDS is rather poor for sample signal no. 2 which is composed of two impulses and two sinusoidal functions. TFDS uses Gabor coefficients of the signal in order to determine the auto terms of the signal on the WVD plane. Since the Gabor coefficients are obtained using sampled STFT, they also inherit some of the drawbacks of STFT. As demonstrated in Figure 3.5 and 3.6, STFT can not give good time and frequency resolutions at the same time because the resolution of the window function in time and frequency domains are bounded by uncertainty principle. Figure 3.22 shows TFDS of order 0 and of order 3 for sample signal no. 2. Performance of AGR is much better in this case because the elementary functions used in AGR have variable variance.

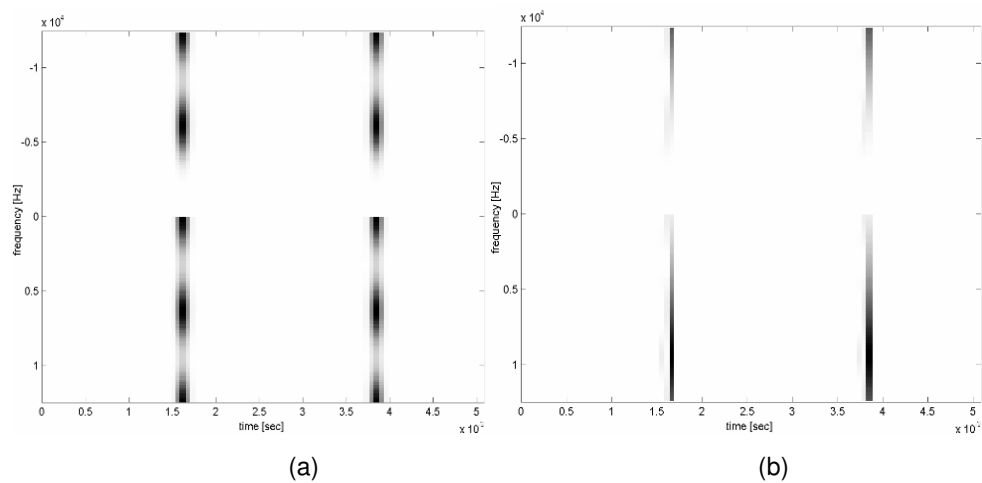


Figure 3.21: (a) TFDS of order 0, (b) TFDS of order 3

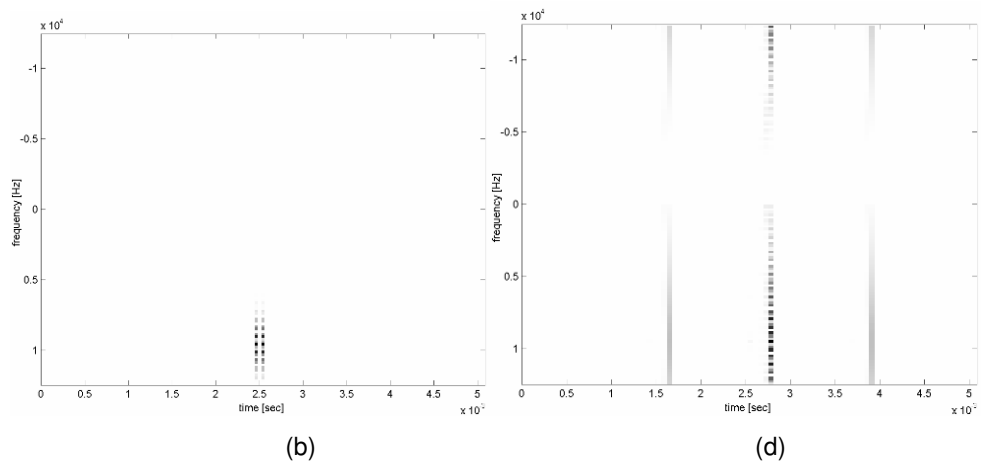


Figure 3.21: (cont'd) (c) P of order 15 and (d) TFDS of order 15 of sample signal no. 3

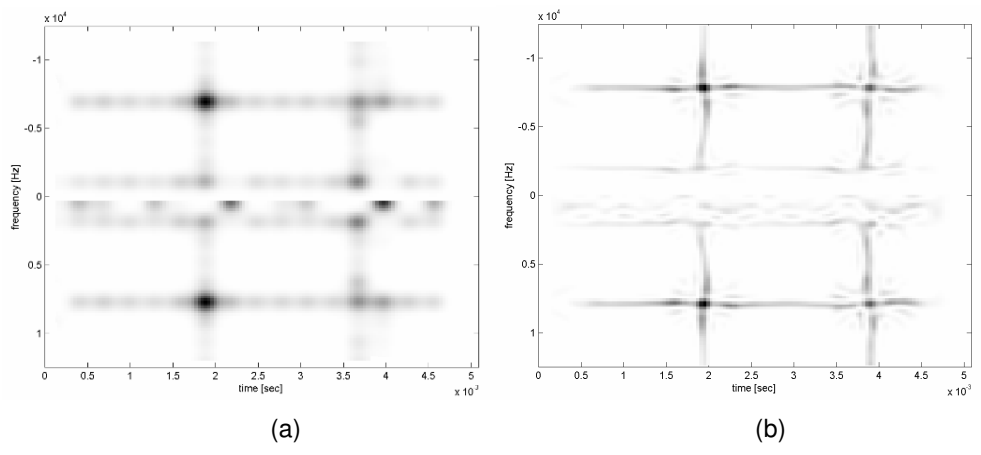


Figure 3.22: (a) TFDS of order 0 and (b) TFDS of order 3 for sample signal no. 2

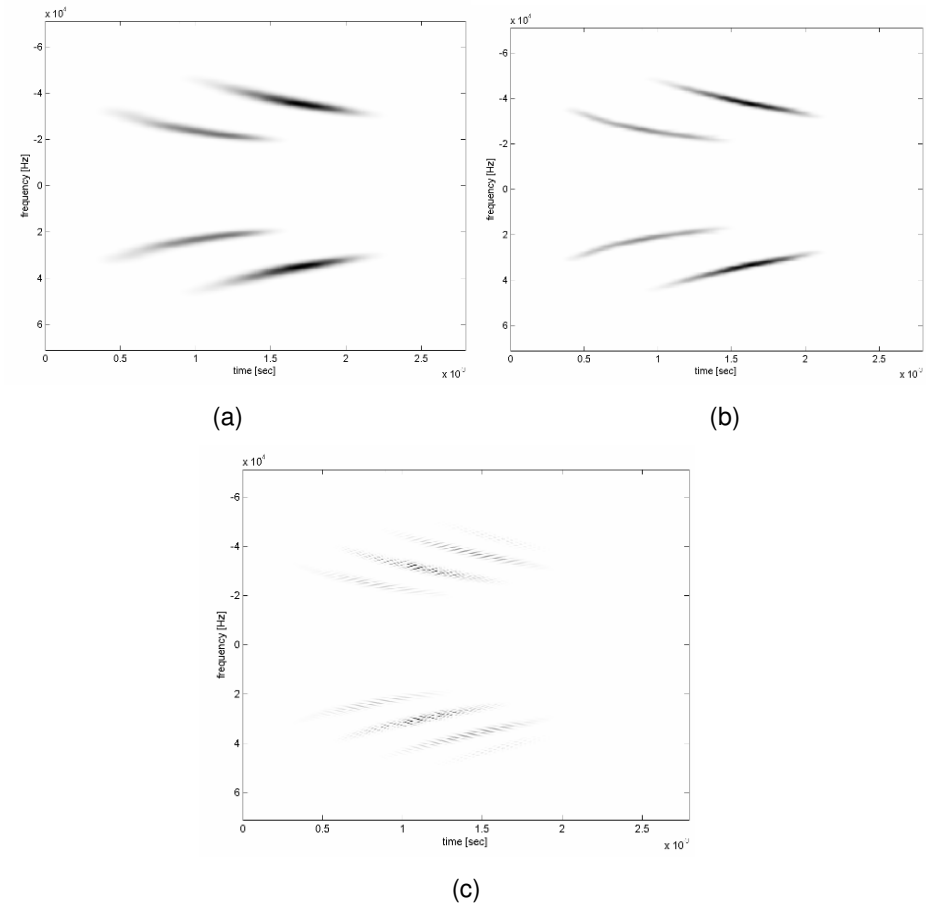


Figure 3.23: (a) TFDS of order 0, (b) TFDS of order 4 and (c) TFDS of order 20 for the bat signal

The bat signal successfully represented with TFDS as shown in Figure 3.23. Better mapping of chirp type signals is possible with TFDS when compared with AGR.

## **CHAPTER 4**

### **APPLICATION OF JOINT TIME-FREQUENCY TRANSFORMS TO RADAR IMAGERY**

#### **4.1 Introduction**

In this chapter, joint time frequency methodologies are applied to the stepped frequency radar imaging system.

#### **4.2 Radar Imaging Using Joint Time-Frequency Transforms**

The time frequency properties of the joint time-frequency transform are very useful to achieve superior resolution and unbiased estimation of the instantaneous frequency spectrum [9]. By replacing the conventional Fourier transform with a joint time frequency transform, two dimensional range-Doppler Fourier frame becomes three dimensional time-range-Doppler image cube. The Doppler shift due to the complex motion of the target can be treated as time-invariant for the each frame encapsulated in the image cube [14]. Therefore, the necessity of a Doppler tracking algorithm is meaningless for a radar imaging system that uses joint time-frequency transforms for target imaging.

Figure 4.1 explains the structure of a radar imaging system with joint time-frequency transform.

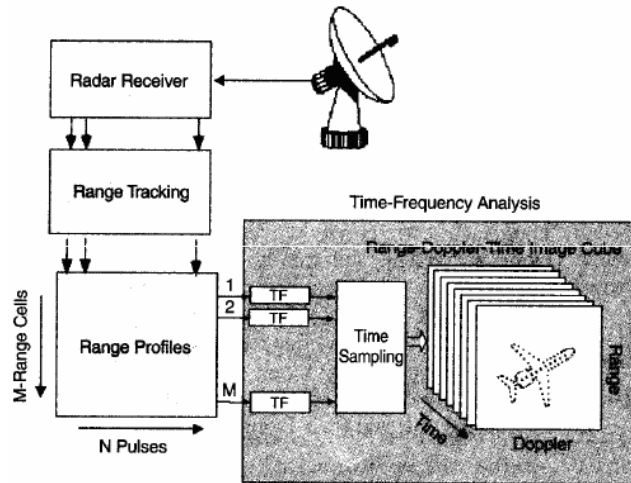


Figure 4.1: The structure of a radar imaging system with joint time-frequency transform [9]

When compared with Figure 2.5, only difference is each range bin is processed with time-frequency transform.

### 4.3 Results

In following sub-chapters simulation results are given.

### 4.3.1 Single Stationary Point Scatterer

The first example used in the simulations is the single stationary point scatterer located at  $x = 1000$  m. and  $y = 0$  m. in the image projection plane. The radar sensor is located at the origin of the coordinate system. This data set is used to verify the step frequency modulated radar simulation system.

Range profiles are obtained by taking inverse Fourier transform of each burst as indicated in Figure 2.5. As it can be seen from Figure 4.5, for single stationary scatterer case, range profiles are composed of impulses at the range bin corresponding to the range of the scatterer. In order to obtain the image using conventional imaging, discrete Fourier transform of each range bin is taken. Since the discrete Fourier transform of the constant function is an impulse, we can identify the scatterer.

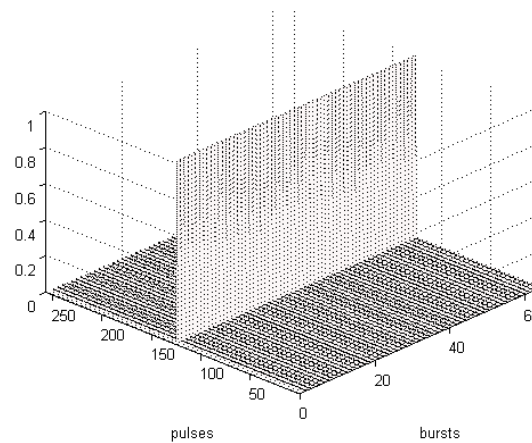


Figure 4.2: Range profile of single stationary point scatterer

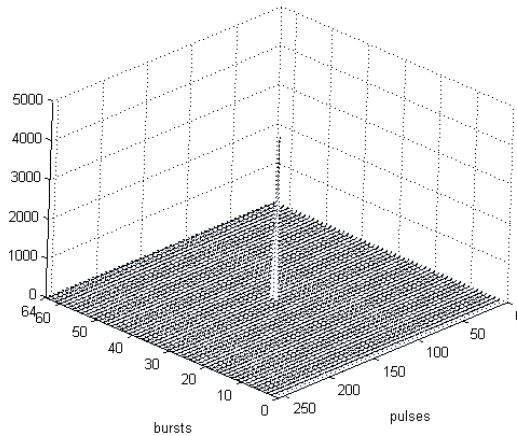


Figure 4.3: Surface plot of the radar image of single stationary point scatterer using Fourier transform

### 4.3.2 Two Stationary Point Scatterers at Different Ranges

Second data set generated is used for similar purposes as in the single point scatterer case. It contains two different stationary scatterers placed at different ranges on image projection plane. The first scatterer is located at  $x = 1000$  m. and  $y = 0$  m. and the second scatterer is located at  $x = 1010$  m. and  $y = 0$  m.

Similar to the single scatterer case explained in chapter 4.3.1 in this case two constant functions can be seen on range profiles. Therefore, two different scatterers can be identified on Figure 4.5

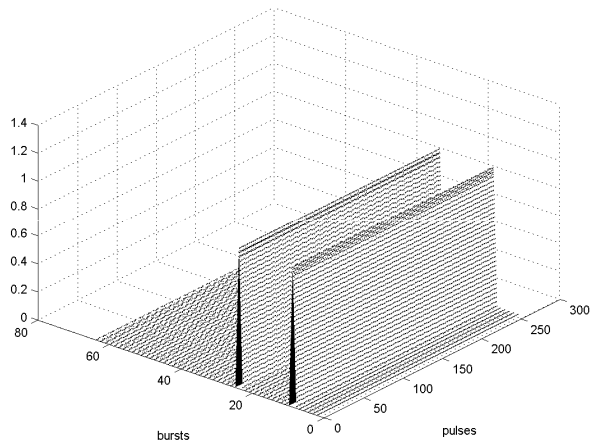


Figure 4.4: Range profile of two stationary scatterers at different ranges

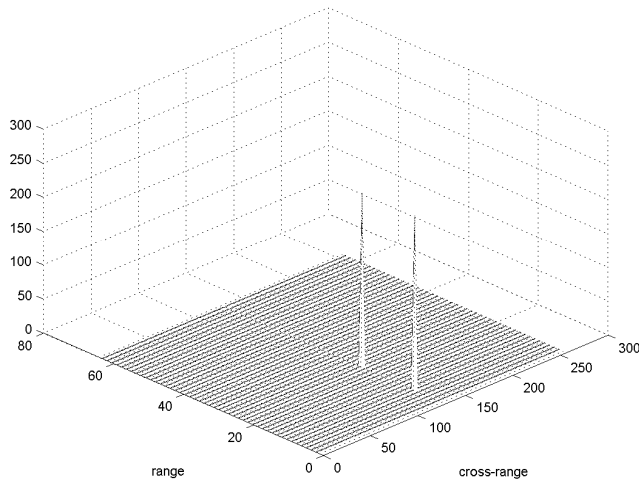


Figure 4.5: Conventional radar image of two stationary scatterers at different ranges

,

### 4.3.3 Two Point Scatterers at Different Cross Ranges

The third set is again composed of two scatterers as in 4.3.2. However, this time only one of the scatterers is stationary. The other scatterer rotates around the other one in order to verify if the system can generate the Doppler shift and therefore, cross-range resolution. The scatterers are separated 5 m. in image projection plane.

In order to obtain two impulses as a result of a discrete Fourier transform operation, the waveform must be a sinusoidal function. This is the case for Figure 4.6. Phase shift caused by Doppler shift due to the rotation causes the change in the response of the rotating scatterer. This change triggers the sinusoidal fluctuation in the range profile as shown in Figure 4.6. As the rotation rate increases, frequency of the fluctuation of the range profile also increases. This causes much more separated image signature for the scatterers which can be observed by comparing Figure 4.7 and 4.9. However, as rotation rate increases, the rotating scatterer drift out from the initial range cell it is located. Moreover, time varying nature of the Doppler shift becomes more visible, which causes the degradation shown in Figure 4.8. As a result, blur is observed at the rotating scatterer signature shown in Figure 4.9.

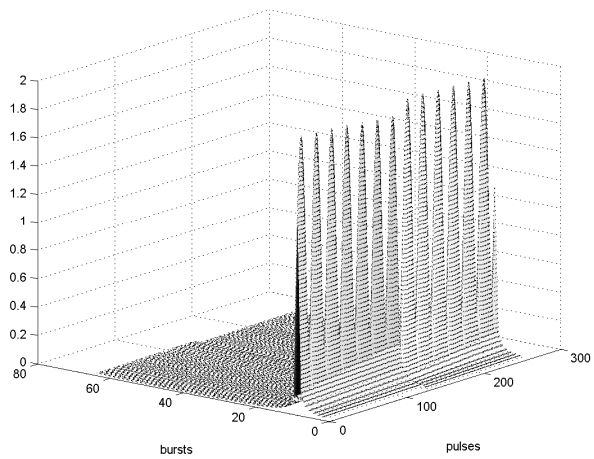


Figure 4.6: Range profiles of two scatterers at same range, separated 5m in cross-range, rotation rate is 3 deg/sec

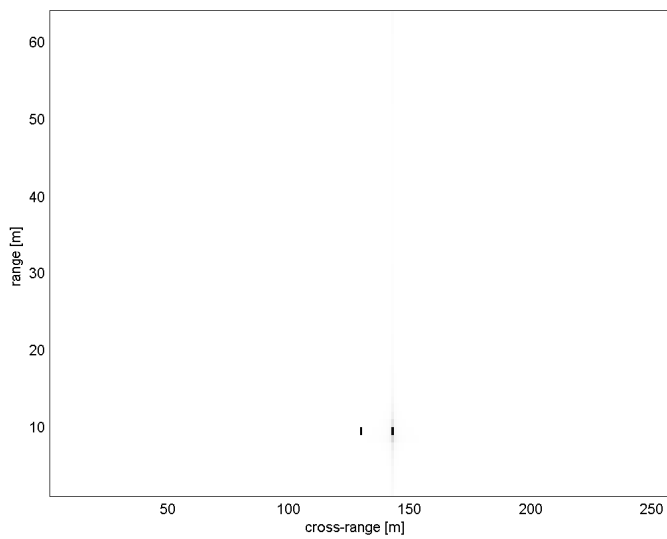


Figure 4.7: Conventional image of two scatterers at same range, separated 5m in cross-range, rotation rate is 3 deg/sec

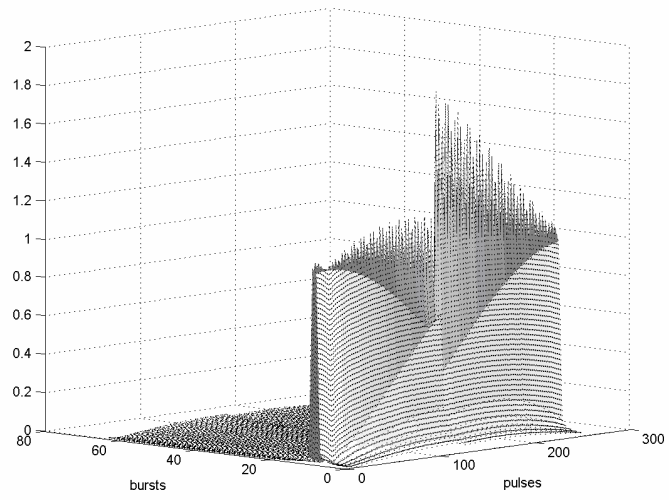


Figure 4.8: Range profiles of two scatterers at same range, separated 5m in cross-range, rotation rate is 18 deg/sec

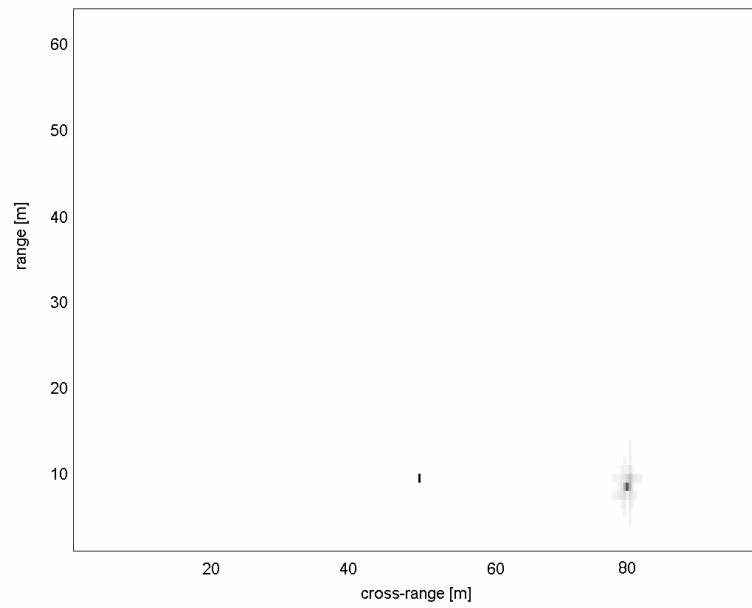


Figure 4.9: Conventional image of two scatterers at same range, separated 5m in cross-range, rotation rate is 18 deg/sec

#### 4.3.4 Rotating Mig-25 Simulation

The time-frequency transform imaging techniques are applied to the data provided by V.C. Chen at <http://airborne.nrl.navy.mil/~vchen/data/>. This data is composed of 128 point scatterers. The Stepped Frequency Radar used for the simulation operates at 9GHz and has a bandwidth of 512MHz. For each pulse, 64 complex range samples were saved. The file contains 512 successive pulses. The Pulse repetition frequency is 15KHz. Basic motion compensation processing without polar reformation has been applied to the data without pulse compression. The target rotates with 10 deg/sec.

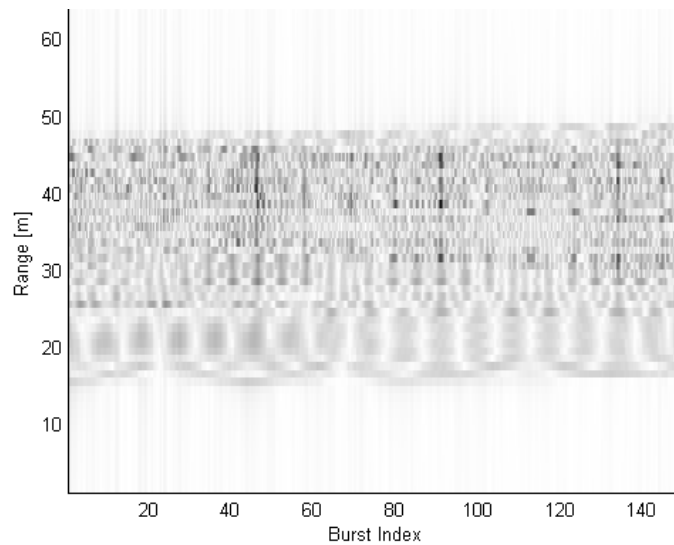


Figure 4.10: Range profile for Mig-25 simulation

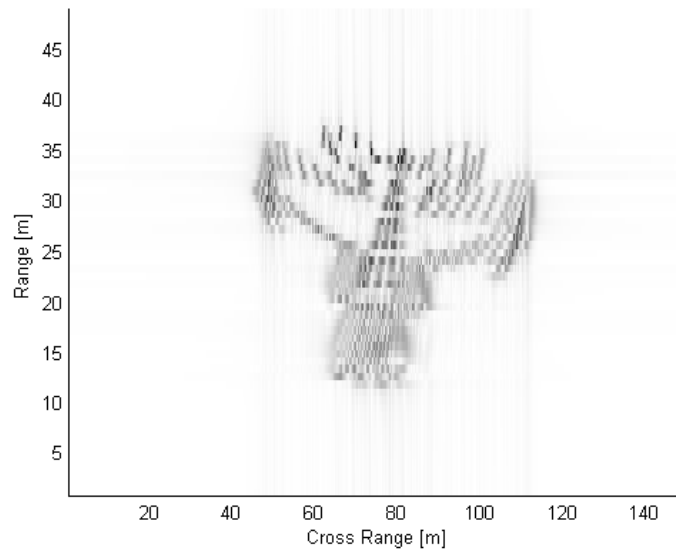
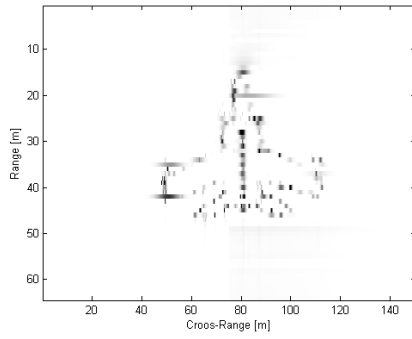
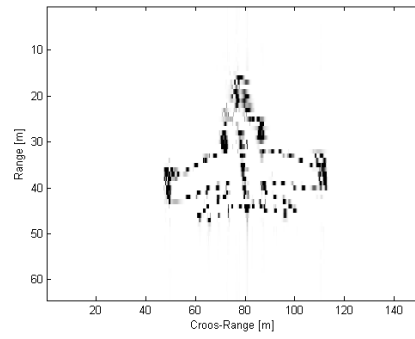


Figure 4.11: Image of Mig-25 simulation using Fourier Transform

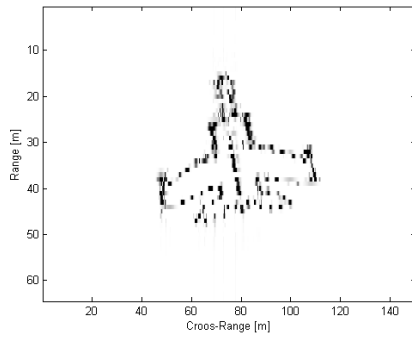
The blurring effect of rotation is completely removed using AGR. This can be easily seen by comparing Figure 4.12 and 4.11. This is also the case for TFDS, for which the results are given in Figure 4.13. However, results obtained using TFDS has poorer image quality when compared to images obtained using AGR.



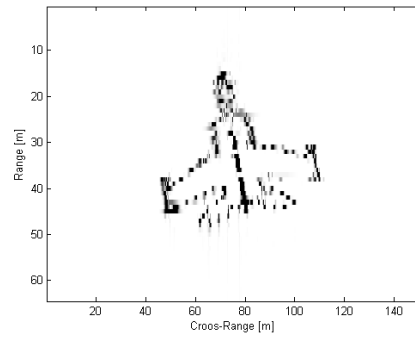
(a)



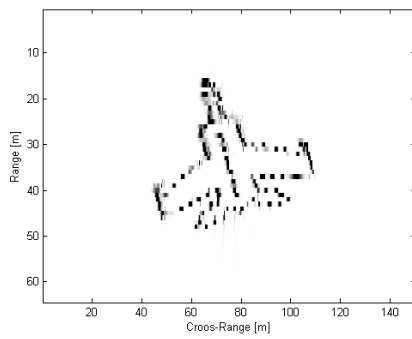
(b)



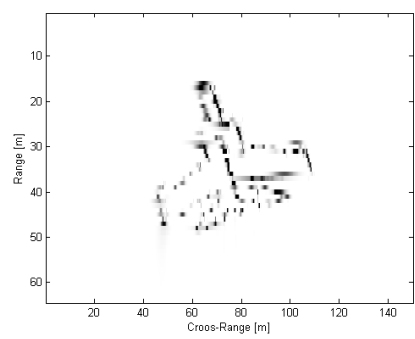
(c)



(d)



(e)



(f)

Figure 4.12: Images of Mig-25 generated using AGR

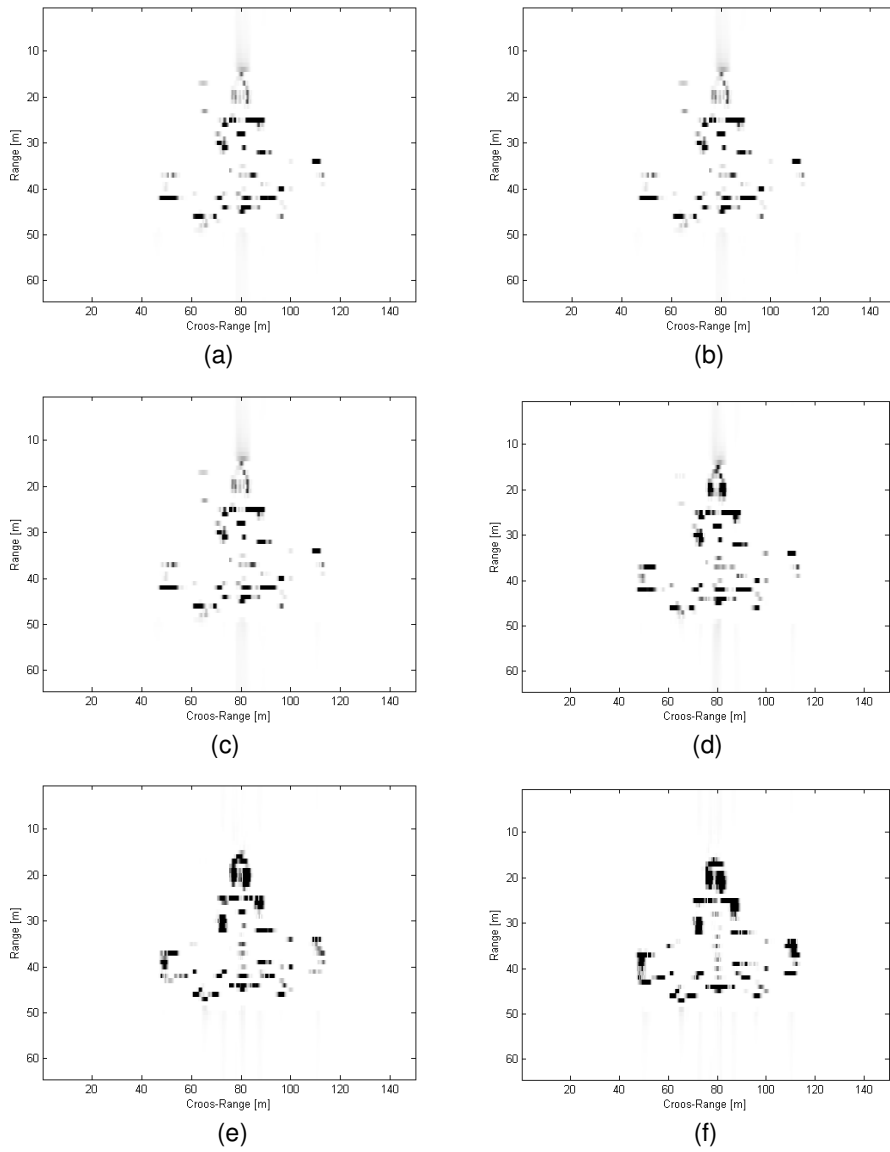


Figure 4.13: Images of Mig-25 generated by using TFDS of order 3

### **4.3.5 Target with Translational Motion and Velocity Fluctuation**

This data set is generated using the point scatterer model shown in Figure 4.14. Although the scatterers in the model can be represented in two dimensions, the simulation for the data set has done in three dimensions. The scatterer located at (0, 0) in the Figure is chosen as reference scatterer and initially it is located at (70, 1600, 100) in meters and the other scatterers of the model placed according to this reference scatterer. The radar sensor is located at the origin of the three dimensional coordinate system. The target moves with a speed of  $v=120$  m/s at  $z=100$  m plane with an angle of 130 degrees to y-axis on this plane. A sinusoidal velocity fluctuation is added in order to add a small phase error to return signal. This will cause an additional degradation in the resulting conventional image. Figure 4.15 shows the location of the target in radar coordinate system and Figure 4.16 is the plot of the speed profile of the target during the observation time.

The radar used in this simulation is assumed operating at 9 GHz and frequency step size of 2.35 MHz. 64 pulses are used in each bursts and 256 bursts are used to generate a total observation time of 0.819 seconds.

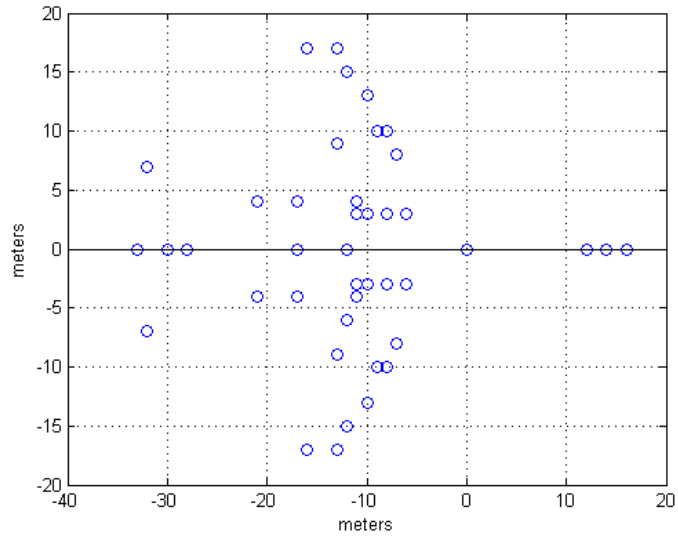


Figure 4.14: Point scatterer model of an aircraft

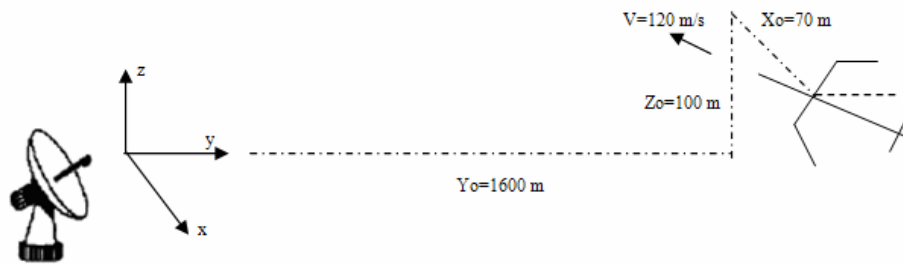


Figure 4.15: Sketch of the initial position of the target

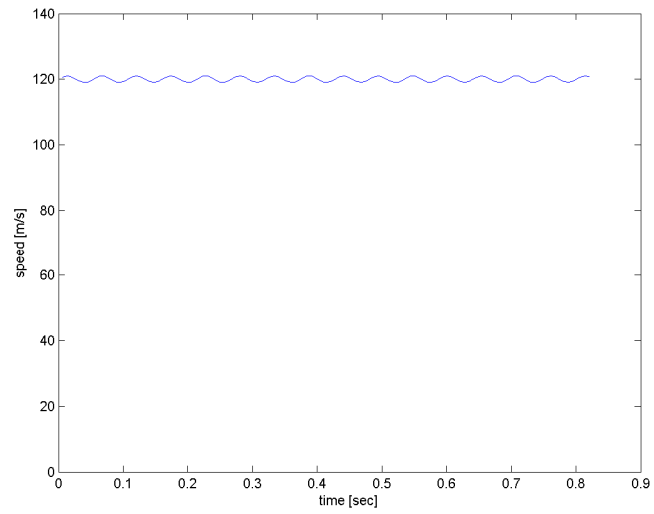


Figure 4.16: Speed of the target vs. Time

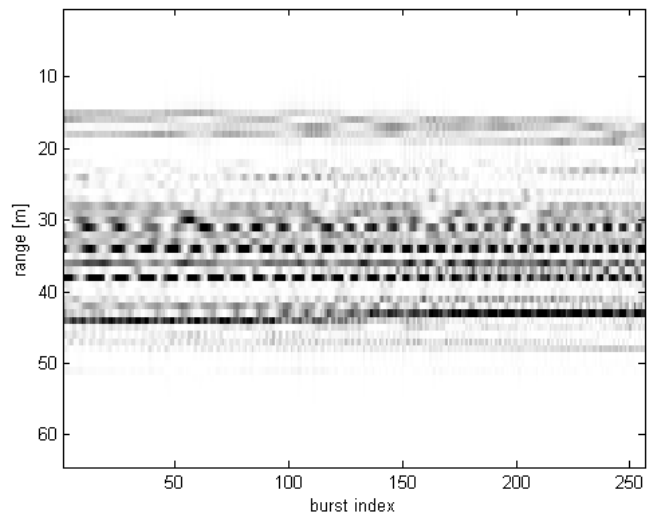


Figure 4.17: Range profile of target with fluctuating translational speed

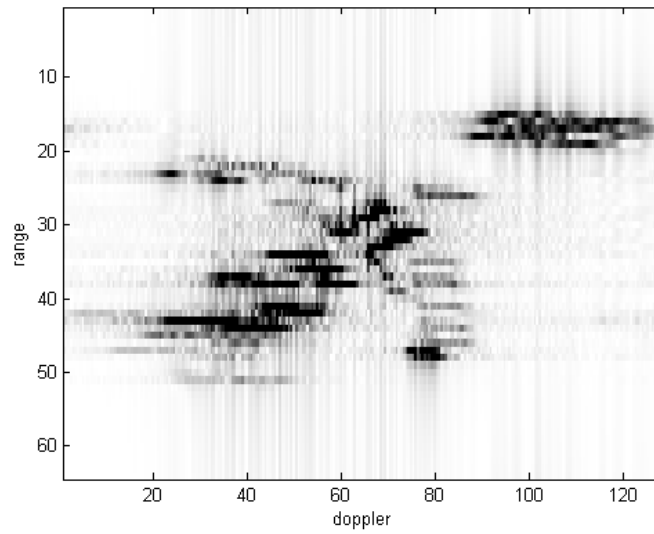


Figure 4.18: Image of target with fluctuating translational speed using Fourier Transform

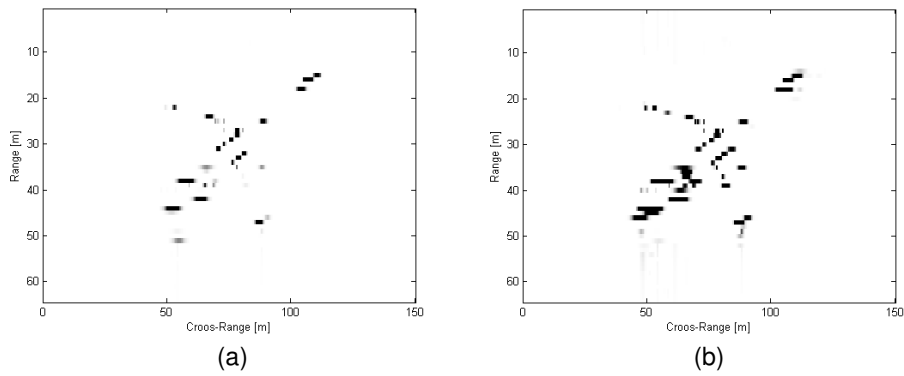


Figure 4.19: Images of target with fluctuating translational speed using AGR

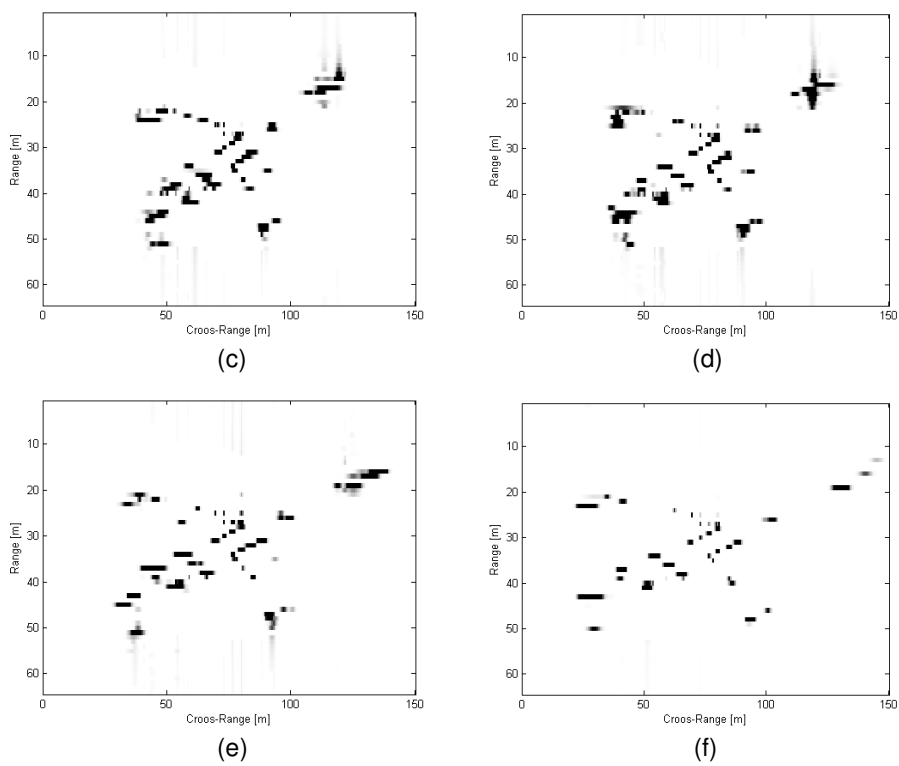


Figure 4.19: (Cont'd) Images of target with fluctuating translational speed using AGR

The conventional image obtained again suffers from blur as shown in Figure 4.18. Both TFDS and AGR images selected from the image cubes generated by these time-frequency transforms reduces the blurring as shown in Figure 4.19 and 4.20.

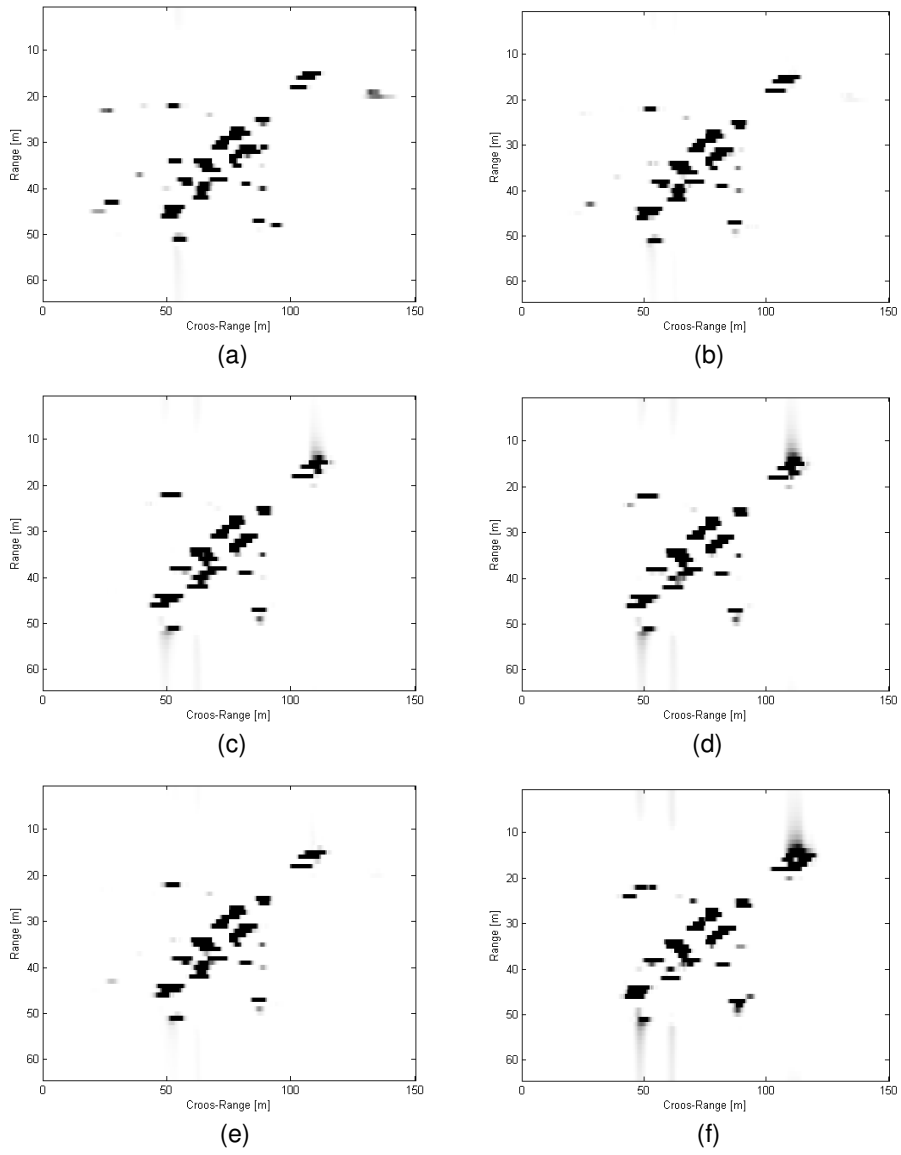


Figure 4.20: Images of target with fluctuating translational speed using TFDS of order 3

### 4.3.6 Measured Data Set

In order to verify the algorithms presented here, the measured data set given in the web page <http://airborne.nrl.navy.mil/~vchen/tftsa.html> (accessed January 14, 2007) is used. The data is composed of the range profiles for a B727 aircraft. The stepped frequency radar used in the measurement has a center frequency of 9 GHz. Total number of bursts is 128 and each burst contains 128 pulses with different frequencies. Bandwidth of each burst is 150 MHz. therefore range resolution of the image is 1 meter. No information on the effective rotation rate of the target and pulse repetition interval of the radar is provided. As a result, cross-range resolution, sample times are not known. Therefore Doppler axes of the images generated are presented as cross-range samples.

Figure 4.21 and Figure 4.22 show the range profiles and the conventional image respectively. As it can be seen from Figure 4.22, unlike simulated data sets, image is noisy. Although the systematic analysis of the system under noise is not evaluated in this thesis, some conclusions may be drawn. Reflections from body and tail parts of the aircraft are much more visible in this data set when compared with nose or wing parts.

Figure 4.23 shows images obtained by using AGR. The body and the tail parts can be identified from the figures as expected. Since the basis functions are adaptively selected in AGR, only the noise around the dominant responses is leaked into the images. Again the resolution is increased and blurring and degradation of the images are decreased visibly.

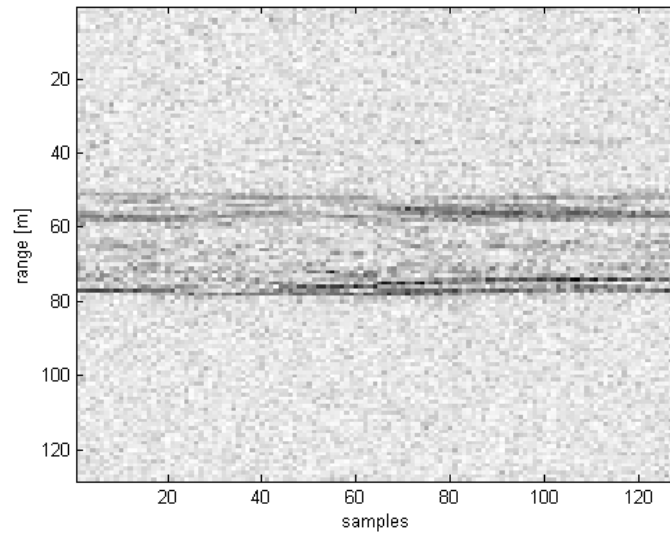


Figure 4.21: Range Profile of measured B727 aircraft

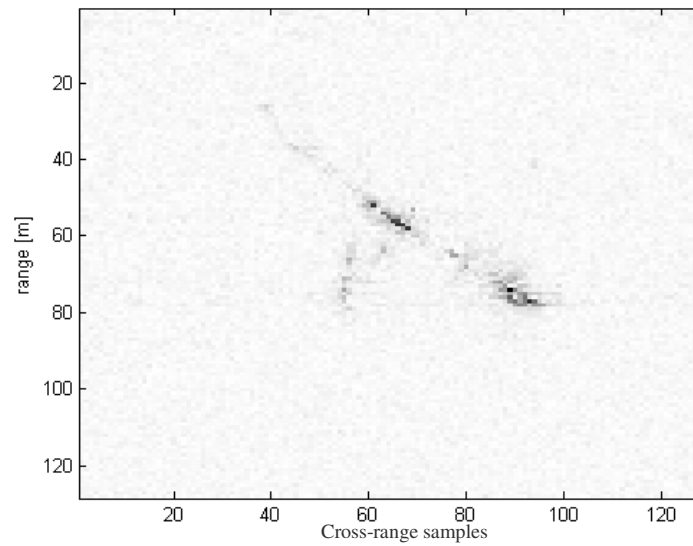


Figure 4.22: Image of measured B727 aircraft using Fourier Transform

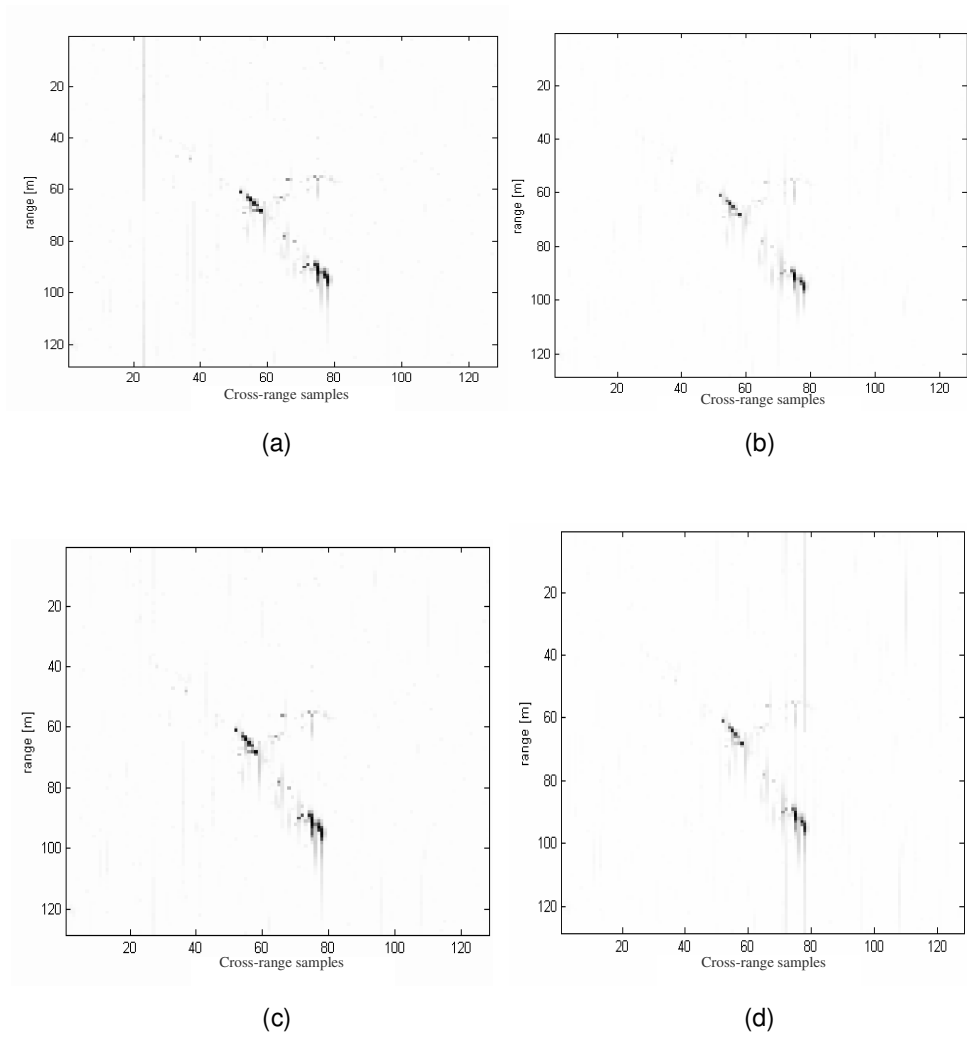


Figure 4.23: Images of measured B727 aircraft using AGR

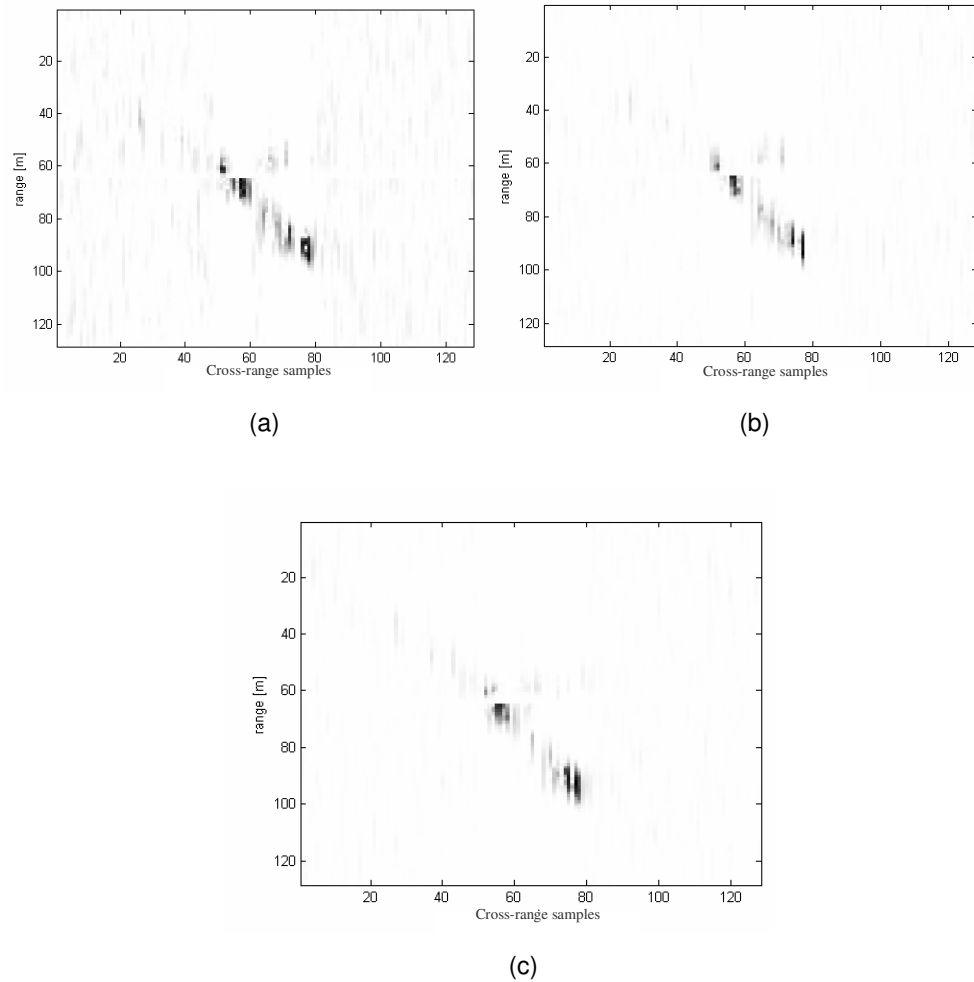


Figure 4.24: Images of measured B727 aircraft using TFDS of order 3

Figure 4.24 shows images obtained by using TFDS. When compared with AGR, TFDS has again poorer image quality as in the simulated data case. Moreover TFDS image cube contains images which possess the noise similar to the conventional image case as shown in Figure 4.24 (a). Again TFDS spent more time than the AGR.

#### 4.4 Comparison of the Joint Time Frequency Imaging Methods

Both TFDS and AGR are successful compared to the conventional algorithm when image quality is considered. The effect of time-varying Doppler effect and blurring are completely removed from the image. However, AGR implementation yields better results than TFDS of order 3 and 4. As indicated in [9], TFDS gives satisfactory resolution but it is far away from the image quality of AGR.

Imaging times for conventional method, AGR and TFDS of order 3 are given for rotating Mig-25 and target with translational motion simulations in table 4.1.

Table 4.1: Imaging times for simulations

	Conventional Imaging	AGR	TFDS (3)
Mig-25	0.016	95.073	581.314
Target with Translational motion	0.009	26.891	367.224
Measured Data Set	0.009	24.475	410.288

Although their superior performance of image quality, time-frequency transform methodologies consume times to generate image cubes that can not be compared with the conventional methodology. There are several propositions to reduce the time of AGR [28], [29] but they can not achieve the speed of Fourier transform.

Besides its lower image quality, TFDS consumes huge amount of time when compared with AGR. Although the algorithm has some improvement opportunities like using look-up tables for elementary functions or using the symmetry of elementary functions [9], basically those methodologies does not reduce the computational complexity of the algorithm.

This comparison shows that AGR is superior to TFDS.

## CHAPTER 5

### CONCLUSIONS

Inverse Synthetic Aperture Radar (ISAR) is a two-dimensional imaging radar. It uses target's own motions to retrieve range-Doppler information of targets. The distribution of the reflectivity mapped on range-Doppler plane is referred to as an ISAR image. In this work, conventional imaging method and two advanced joint time-frequency imaging methods are investigated. In order to extract the Doppler shift from the raw data, the fastest and simplest method is conventional Fourier transform methodology. However, the efficiency of the methodology drastically drops when the target under examination has relatively fast and complex motion profile. The time-varying nature of the Doppler shift begins to possess more and the scatterers start to drift out from their initial range cells under complex motion circumstances. More complex motion compensation schemas must be applied to the data in order to obtain better image quality using Fourier transform.

Image quality can be improved highly using joint time frequency transforms instead of Fourier transform and the need for complex motion compensation algorithms totally disappear. Two different joint time-frequency techniques are implemented for this purpose, namely Adaptive Gaussian Representation (AGR) and Time Frequency Distribution Series (TFDS).

TFDS decomposes the signal into elementary functions using Discrete Gabor Transform (DGT). Coefficients of DGT hold the information of the auto-terms of the signal in the form of modulated Gaussian signals. Therefore, auto-terms and the cross-terms of the WVD can be controlled on WVD plane. Therefore, obtaining a high-resolution time-frequency transform which is free of cross-term interference becomes possible.

AGR with Coarse-to-Fine search methodology finds the elementary functions by adaptively searching the signal for the best fitted elementary function. Since the elementary functions that are adaptively computed has variable variance, this representation gives the best image quality. However, signals with variable frequency content like chirp-type signals, can not be represented effectively with this representation.

Application of the radar imagery shows the main drawback of these two methods. Although superior image quality, time spent by the AGR and TFDS has an order that can not be compared with the conventional methodology. Especially TFDS has unacceptable processing time. Therefore, possibilities to reduce the computational complexity of these two representations must be examined. The methods to reduce the time for TFDS is given in [9], however, those recommendations do not reduce the computational complexity of the implemented algorithm. Therefore the upper bound for the TFDS algorithm is still the same after those improvements. To implement AGR more effectively, developed methodologies sacrifices from the image quality [29], [28].

Adaptive joint time-frequency transforms can also be applied to the motion compensation algorithms for the conventional imaging methodology. As a future work, analysis of image quality and processing time for such a configuration for imaging radar would be interesting.

## REFERENCES

- [1] V.C. Chen, H. Ling, "Time Frequency Transforms for Radar Imaging and Signal Analysis", Artech House, 2002
- [2] M. I. Skolnik, "Introduction to Radar Systems", McGraw Hill, 1980
- [3] V.C. Chen, H. Ling, "Joint Time Frequency Analysis for Radar Signal and Image Processing", IEEE Signal Processing Magazine, Vol. 16 ,Issue 2, pp. 91-83, 1999
- [4] A. Zyweck, R.E. Bogner, "High Resolution Radar Imagery of the Mirage III Aircraft", IEEE Transactions on Antennas and Propagation, Vol. 42 Issue 9, pp. 1356-1361, 1994
- [5] D. L. Mensa, "High Resolution Radar Cross-Section Imaging", Artech House, 1991
- [6] V. C. Chen, S. Qian, "Joint Time-Frequency Transform For Radar Range-Doppler Imaging", IEEE Transactions On Aerospace And Electronic Systems, Vol. 34, No. 2, pp. 486-499, 1998
- [7] D. A. Ausherman, A. Kozman, J. L. Walker, H.M. Jones, E. C. Poggio, "Developments in Radar Imaging", IEEE Transactions on Aerospace and Electronic Systems, Vol. AES-20, No. 4, pp. 363-400 1984
- [8] Y. Wang, H. Ling, V. C. Chen, "ISAR Motion Compensation Via Adaptive Joint Time-Frequency Technique", IEEE Transactions On Aerospace And Electronic Systems, Vol. 34, No. 2, pp. 670-677 1998
- [9] S. Qian, D. Chen, "Joint Time-Frequency Analysis – Methods And Applications", Prentice Hall, 1996
- [10] S. Qian, D. Chen, "Discrete Gabor Transform", IEEE Transactions On Signal Processing, Vol. 41, No. 7, pp. 2429-2438, 1993

- [11] V. C. Chen, "Adaptive Time-Frequency ISAR Processing", SPIE, Vol. 2845/133 pp. 133-140
- [12] S. Qian, D. Chen, "Decomposition Of Wigner-Ville Distribution And Time-Frequency Distribution Series", IEEE Transactions On Signal Processing, Vol. 42, No. 10, pp. 2836-2842, 1994
- [13] D. R. Wehner, "High-Resolution Radar", 2<sup>nd</sup> ed., Artech House, 1995
- [14] V. C. Chen, S. Qian, "Joint Time-Frequency Transform For Radar Range-Doppler Imaging", IEEE Transactions On Aerospace And Electronic Systems, Vol. 34, No. 2, pp. 486-499, 1998
- [15] V. C. Chen, W. J. Micelli, "Simulation of ISAR Imaging of Moving Targets", IEEE Proceedings on Radar, Sonar and Navigation, Vol. 148, No. 3, pp. 160-166, 2001
- [16] A. W. Rihaczek, S. J. Hershkowitz, "Radar Resolution and Complex Image Analysis", Artech House, 1996
- [17] L. Cohen, "Time – Frequency Analysis", Prentice Hall, 1995
- [18] D. Gabor, "Theory Of Communication", J. IEE (London), Vol. 93, No. 3, pp. 429-457, 1946
- [19] H. E. Jensen, T. Hoholdt, J. Justesen, "Double-Series Representation Of Bounded Signals", IEEE Transactions On Information Theory, Vol. 34, No. 4, pp. 613-624, 1988
- [20] P. P. Vaidyanathan, "Multirate Systems And Filter Banks", Prentice Hall, 1993
- [21] M. Zibulski, Y. Y. Zeevi, "Oversampling In The Gabor Scheme", IEEE Transactions On Signal Processing, Vol. 41, No. 8, pp. 2101-2104, 1993
- [22] M. Zibulski, Y. Y. Zeevi, "Frame Analysis Of The Discrete Gabor Scheme", IEEE Transactions On Signal Processing, Vol. 42, No. 4, pp. 942-945, 1994

- [23] S. Li, D. M. Healy Jr., "A Parametric Class Of Discrete Gabor Expansions", IEEE Transactions On Signal Processing, Vol. 44, No. 2, pp. 201-211, 1996
- [24] M. J. Bastiaans, "Gabor's Expansion Of A Signal Into Gaussian Elementary Signals", Proceedings of IEEE, Vol. 68, No. 4, pp. 538-539, 1980
- [25] M. J. Bastiaans, "On The Sliding Window Representation In Digital Signal Processing", IEEE Transactions On Speech, Acoustics, And Signal Processing, Vol. ASSP-33, No. 4, pp. 868-873, 1985
- [26] J. Wexler, S. Raz, "Discrete Gabor Expansions", Signal Processing Vol. 21, No. 3, pp. 200-207, 1990
- [27] S. Qian, D. Chen, "Optimal Biorthogonal Analysis Window Function For Discrete Gabor Transform", IEEE Transactions On Signal Processing, Vol. 42, No. 3, pp. 694-697, 1994
- [28] E. L. Atılgan, "Target Identification Using ISAR Imaging Techniques", Ms Thesis, METU, 2005
- [29] S. G. Mallat, Z. Zhang, "Matching Pursuits With Time-Frequency Dictionaries", IEEE Transactions On Signal Processing, Vol. 41, No. 2, pp. 3391-3415, 1993